Final Report

Project Title: "All-Inorganic, Efficient Photovoltaic Solid State Devices Utilizing Semiconducting Colloidal Nanocrystal Quantum Dots"

Covering Period: April 1, 2008 until September 30, 2011

Date of Report: November 11, 2011

Recipient: Massachusetts Institute of Technology

Award Number: DE-FG36-08GO18007

Contacts:

Vladimir Bulovic
Phone: 617-353-7012
Fax: 617-452-5110
Email: bulovic@mit.edu

Moungi Bawendi
Phone: 617-253-9796
Fax: (617) 253-7030

Executive Summary: We demonstrated robust colloidal quantum dot (QD) photovoltaics with high internal quantum efficiencies. In our structures, device durability is derived from use of all-inorganic atmospherically-stable semiconducting metal-oxide films together with QD photoreceptors. We have shown that both QD and metal-oxide semiconducting films and contacts are amenable to room temperature processing under minimal vacuum conditions, enabling large area processing of PV structures of high internal efficiency. We generated the state of the art devices with power conversion efficiency of more than 4%, and have shown that efficiencies as high as 9% are achievable in the near-term, and as high as 17% in the long-term.

Motivation and Outcomes: Considerable interest in the incorporation of colloidal QDs and other quantum-confined semiconductor structures into photovoltaics (PVs) is due to their broad spectral tunability, strong optical absorption, and ease of processing. QDs made from the II-VI materials such as CdS, CdSe, and CdTe can be tuned in the visible, while IV-VI materials such as PbS and PbSe exhibit band-edge responses in the IR, even beyond $\lambda = 2000$ nm wavelength. As solution processable perfect crystals of tunable band gap, colloidal QD-PVs have a remarkable potential to advance the photovoltaic technology.

- The broad tunability of the spectral response of QD-PV enables design of stacked QD-PV structures of varying band gaps.
- As a stand-alone technology, QD-PVs can be used as PVs on flexible substrates, amenable to ease of processing and less costly deployment, while maintaining atmospheric robustness.
- Alternatively, QD-PVs can be deposited on top of existing solid state PVs to form tandem PV geometries of boosted efficiency, while eliminating the need for additional substrates or packaging for QD-PV deposition.

Using our PVs as a test bed of physics, we charted out the operating principles of photosensitive devices containing inorganic nanocrystal QDs. To date, we

demonstrated high quantum efficiency photosensitive devices that utilize nanocrystal QD monolayers and multilayers sandwiched between organic and inorganic semiconducting films. These unique device structures enabled us to test physical processes in solid-state layers of single QD thickness. Specifically, we performed the first ever measurements of parameters such as built-in fields at the QD heterojunction, relative QD electron affinity and ionization potentials, and the quantum efficiency of QD exciton dissociation as a function of QD size (electron energy alignment) and QD shell thickness. These are the governing parameters of all heterogeneous QD/ semiconductor photosensitive devices and insights gained enabled us to exceed the initially targeted performance. We generated the state of the art devices with power conversion efficiency of more than 4%, and have shown that efficiencies as high as 9% are achievable in the near-term, and as high as 17% in the long-term.

All the Tasks Projected in the Statement of Objectives (SOPO) for the Entire Program have been Completed and in Some Cases Exceeded:

Task 1: *Synthesize colloidal QDs to generate QD size distribution and QD band structure progression that will be interfaced with metal-oxide thin films to establish the likely band-to-band offsets at the QD/metal-oxide heterointerface.*

Accomplished. Initial measurements have recently been accomplished and published for QD/organic semiconductor structures [Arango *et al.*, *Nano Lett.* 9, 860 (2009)]. Clear tunability of the QD absorption band edge is translated into tunable photoresponse of QD-PVs. Initial work on the QD/metal-oxide interfaces was accomplished in the form of a PbS QD / SnO_2 heterojunction, demonstrating a photodetector with gain.

Task 2: *Perform internal photoemission measurements of QD/metal-oxide heterostructures to establish heterojunction band offsets. The energy band alignment at the heterointerface determines the ability to dissociate photogenerated QD excitons.*

Accomplished. The functional operation of the PbS/SnO2 photodetectors, confirms that these are Type II heterojunction devices. Our recent publication [Brown *et al.*, *Nano Lett.* 11, 2955-2961 (2011)] further confirms the band structure at the heterojunction and the contacts.

Task 3: *Establish a benchmark performance of all-inorganic QD/metal-oxide-PV structures.*

Accomplished. At the end of Phase I we reported on demonstrating PbS QD PVs with 1.68% power conversion efficiency in an archetype PV structure. At the end of Phase II we improved that performance to 4% and estimated possible improvemnets that can reach 9% in the near-term and 17% in the long-term.

Task 4: *Demonstrate QD-PVs with printed QD film on top of metal-oxides.*

Accomplished. We demonstrated spray-coated QD-PV structures, enabling us to efficiently use QDs and to deposit them over larger areas. Furthermore, the processing time of the spray-coated structures can be significantly shorter than

for the spun-cast structures and the film thickness should be able to be maintained over large areas.

Task 5: *Develop chemical/thermal QD film treatments to improve charge carrier transport through QD films.*

Accomplished. We utilized chemical treatment of QDs to planarize QD and metal oxide films, to minimize the pinhole density and alleviate device shorting. We also established the consequence of various chemical treatments on the shunt and series resistance of our QD PVs. These findings were published in [Zhao *et al.*, *ACS Nano* 4, 3743-3752 (2010).]

Task 6: *Continue improving the QD fabrication methods by automating the printing setups and generating environmentally enclosed environments for higher control in print quality.*

Accomplished. Environmentally enclosed environments have been generated for deposition of QD films. Benefit of the enclosure to the device performance is evaluated.

Task 7: *Perform ultraviolet photoemission spectroscopy of QD monolayers and multilayers fabricated on conducting surfaces to establish progression of QD band structures.*

Accomplished. We completed the UPS measurements and found them to be less stable that STM measurements that reproducibly generated energy level positions of QD films. This work was detailed in Hummon, *et al.*, *Physical Review B* 81, 115439 (2010).

Task 8: *Examine the influence of the fabrication method on the QD surface dipolar properties (reflected in the QD workfunction measured by UPS and internal photoemission spectroscopy).*

Accomplished. UPS measurements completed.

Task 9: *Fabricate and measure tandem structures of QD-PVs on top of conventional PV cells.*

Accomplished. QD-PVs with transparent contacts were fabricated and measured.

Task 10: Optimize tandem QD-PV structure for the appropriate QD energy gaps.

Examined and Accomplished. The role of QD bandgaps has been elucidated. In our related study inspired by this work [Lunt *et al.*, *Advanced Materials* 23, 5712–5727] we are able to estimate the ultimate practical limits of performance of QD-PVs.

Task 11: *Utilize the knowledge gained to demonstrate high performance single junction QD-PVs.*

Accomplished, with additional improvements in progress. Our present all-metal oxide QD-PV structures demonstrate the highest V_{OC} and fill factor of any QD-PV device. [Zhao *et al.*, *ACS Nano* 4, 3743-3752 (2010).] Our best performing PVs have

power conversion efficiency of 4%, the highest for the multilayer QD thin film structures. [Brown *et al.*, *Nano Lett.* 11, 2955-2961 (2011).]

Task 12: Develop a comprehensive picture of photogeneration processes in QD/metal-oxide PVs.

Accomplished. We developed a comprehensive picture of all-inorganic QD-PV operation as explained in our manuscript that has recently been published in *ACS Nano* and in *Nano Letters*.

Task 13: Demonstrate a stacked structure with two QD-PV cells.

Accomplished. QD-PVs with transparent contacts were fabricated and first attempts in stacking tandem QD-PVs were made.

Significant Accomplishments Within the Whole Program:

Complete list of participants:
Patrick R. Brown, Ni Zhao, Richard R. Lunt, Timothy P. Osedach, Darcy D. Wanger, Liang-Yi Chang, Scott M. Geyer, Maddalena T. Binda, Alexi C. Arango, Moungi G. Bawendi, and Vladimir Bulović

Three of the students/post docs who were trained in this program became professors:

Alexi Arango – Assistant Professor of Physics, Amherst College
Richard R. Lunt – Assistant Professor of Chemical Engineering, Michigan State University
Ni Zhao – Assistant Professor of Electronic Engineering, Chinese University of Hong Kong

Project Overview

Over the past several decades, intensive research efforts have been undertaken to develop low-temperature-processed photovoltaic cells through the use of nanostructured materials including small molecules[1-4], conjugated polymers[5-9] and colloidal nanocrystal quantum dots (QDs)[10, 11]. There has been much progress in improving the power conversion efficiency (η_P) of nanostructured solar cells in the visible-light region with reported efficiencies reaching 6.7%[5, 9]. An important approach toward realizing significant improvements to this performance is to extend the spectral sensitivity of cells to near infrared wavelengths, which contain as much as half of the energy of the solar spectrum. This can potentially be achieved by using colloidal nanocrystal QDs as the light-harvesting material, as their optical band gap can be tuned to a desired range by choosing the appropriate material composition and by controlling nanocrystal size during synthesis[12-14].

Amongst the QD materials PbS and PbSe QDs possess excellent photo-sensitivity in the near-infrared spectrum. Solar cells based on a Schottky barrier formed at the interface of the p-type PbS or PbSe QD films and a metal cathode have been reported[15-18] with η_P's of up to 2.1%[15] under 1-sun AM1.5 test conditions. In these devices, it is suggested that photocurrent is generated by field-assisted charge separation in the depletion region. One limitation of Schottky-

based solar cells is that the open-circuit voltage (V_{OC}), an important metric that directly affects the η_P, is expected to be lower than 0.5 E_g/q,[19] where E_g is the band gap of the semiconducting material and q is the electron charge. A heterojunction solar cell incorporating an electron-transporting/hole-blocking layer between the QDs and the metal cathode could potentially allow for a higher V_{OC}. The challenge in realizing such a device is to find materials that provide an appropriate energy level alignment with the low band gap QDs such that electron injection from QDs to the material is promoted while back electron transfer to the QDs (that would lead to the undesirable electron-hole recombination) is suppressed.

In the present progress report, we describe two approaches for improving the efficiency of photovoltaics based on a *pn* heterojunction between *p*-type colloidal PbS QDs and an *n*-type electron-transporting layer (ETL). First, we describe the fabrication of a PbS QD-based solar cell using a fullerene derivative as the ETL. A thiol treatment and oxidation process are used to modify the morphology and electronic structure of the QD films resulting in devices that exhibit a fill factor (FF) as high as 62%. We also show that for QDs with a band gap of less than 1eV, an open-circuit voltage (V_{OC}) of 0.47 V can be achieved. The power conversion efficiency reaches 1.3% under 1-sun AM1.5 test conditions and 2.4% under monochromatic infrared (λ = 1310 nm) illumination. A consistent mechanism for device operation is developed through a circuit model and experimental measurements, shedding light on new approaches for optimization of solar cell performance by modifying the interface between the QDs and the neighboring charge transport layers.

Second, we demonstrate that improvements in power conversion efficiency may be attained for ZnO/PbS heterojunction quantum dot photovoltaics through the incorporation of a MoO_3 interlayer between the PbS colloidal quantum dot film and the top-contact anode. Through a combination of current-voltage characterization, circuit modeling, Mott-Schottky analysis, and external quantum efficiency measurements performed with bottom- and top-illumination, these enhancements are shown to stem from the elimination of a reverse-bias Schottky diode present at the PbS/anode interface. The incorporation of the high-work-function MoO_3 layer pins the Fermi level of the top contact, effectively decoupling the device performance from the work function of the anode and resulting in a high open-circuit voltage (0.59 ± 0.01 V) for a range of different anode materials. Corresponding increases in short-circuit current and fill factor enable 1.5-fold, 2.3-fold, and 4.5-fold enhancements in photovoltaic device efficiency for gold, silver, and ITO anodes, respectively, and result in a power conversion efficiency of 3.5 ± 0.4% for a device employing a gold anode.

1. Colloidal PbS Quantum Dot Solar Cells with High Fill Factor

In the present work we demonstrate that it is possible to improve both the V_{OC} and the FF of QD/organic bilayer solar cells through modifying the interface properties that govern the charge separation and recombination process in these devices. The bilayer QD/organic solar cells presented in this study consist of an ITO-coated glass substrate on which we deposit a thin film of PbS QDs, which acts as both the light-absorbing and charge-transporting layer. The QD film is then coated with a thin film of a fullerene derivative, [6,6]-phenyl-C61-butyric acid methyl ester (PCBM), which serves as the electron transporting and hole blocking layer. (PCBM was chosen in this work because efficient electron transfer from PbS QDs to PCBM was

demonstrated in a recent study of PbS QD/PCBM photodetectors[22, 23].) To modify the electronic structure of individual PbS QDs and QD thin films in our devices, the QD films are subjected to air annealing, nitrogen annealing, or ozone exposure. Air annealing has previously been used to improve the conductivity of QD films via a doping mechanism[24, 25]. It has also been shown to enhance the V_{OC} and the air stability of PbS QD-based Schottky devices[26 27], where chemical analysis revealed that the performance improvement is related to the formation of PbO and $PbSO_3$ during the air annealing process. However, the mechanism through which these oxidation products affect the charge separation, recombination and transport remains unclear.

Here, for solar cells containing small band gap PbS QDs (Eg < 1.0 eV) that are air annealed and treated with thiols prior to PCBM deposition, we measure a fill factor as high as 62%. Also, a V_{OC} of 0.47 V is achieved for QDs with a band gap of 0.97 eV (after air annealing). This exceeds the V_{OC} value of 0.27 V predicted by the relation $V_{OC} = 0.6$ (Eg/e) – 0.31 as reported in PbSe/ZnO heterojunction solar cells [21]. The η_P for these structures is ~1.3% under 1-sun AM1.5 test conditions and 2.4% under monochromatic infrared light illumination (of wavelength λ = 1310 nm, corresponding to E=0.95 eV). We also demonstrate that further improvement of the η_P is possible with ozone treatment (reaching a η_P of 1.7% under AM1.5, but with lower V_{OC} and FF). Devices made with and without oxidation treatments are studied through measurements of optical absorption, quantum efficiency, shunt and series resistances, light intensity dependence and charge recombination lifetime. The results suggest that the use of the bilayer structure and the oxidation treatment enhances the shunt resistance of the device by suppressing the charge recombination process, resulting in a high V_{OC} and FF.

Device Performance

A schematic of our device structure is shown in Figure 1a. The long oleic acid ligands on the as-synthesized QDs were first replaced by butylamine ligands in solution, which were then exchanged by ethanedithiol ligands after formation of QD films to improve charge transport properties and decrease solubility of the films. The QD layer is then processed in one of four different ways prior to the deposition of PCBM: no further treatment ("pristine"), annealed in air ("air annealed") or nitrogen atmosphere ("N_2 annealed") at 110˚C for 30 minutes, or treated in an ozone environment for 6 seconds ("ozone treated"). For the annealed devices we applied a post-annealing ethanedithiol (EDT) solution treatment to the QD layer for 30 seconds, which has been observed to lead to a higher photocurrent in our PbS QD/PCBM devices. Notably, this treatment has the effect of reducing the conductivity of air-annealed films of PbS QDs, presumably due to it passivating surface states on QDs and therefore reducing the carrier concentration. Meanwhile, the increase of the photocurrent in the solar cell devices indicates that the post-annealing treatment may increase the exciton lifetime and reduce the density of electron traps in PbS QDs, which should increase electron transfer to the PCBM film.

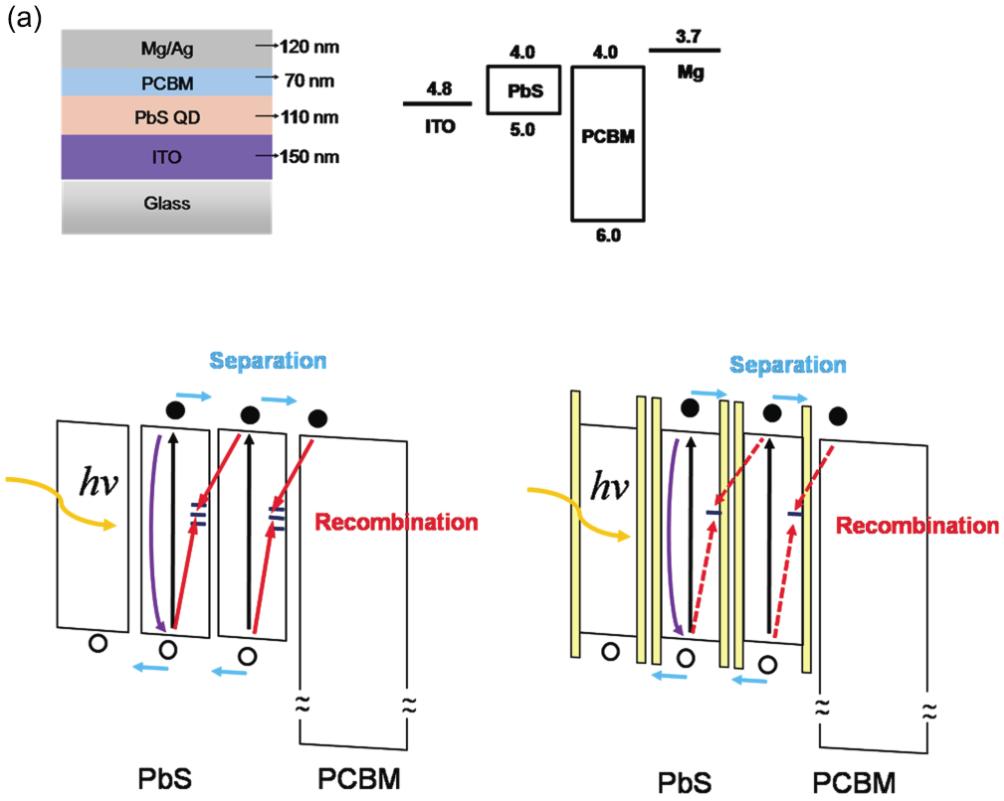

Figure 1. (a) Schematic of the bilayer solar cell structure and the energy level diagram of device components referenced to the vacuum level. (b) Illustration of the charge flow mechanism in the pristine (left) and air annealed (right) PbS QD/PCBM devices. The black arrows denote the exciton generation process, the purple arrows denote the geminate electron-hole pair recombination process, the blue arrows denote the charge separation process, and the red arrows denote the bimolecular recombination process (assisted by midgap states). The thin wider band gap layers (yellow) that surround each QD in the right figure represent the oxide compounds, and the dashed red arrows indicate a suppressed charge recombination via the bimolecular process. Note that the charge separation and recombination occur in both bulk PbS QD layer and at the PbS QD/PCBM interface.

The current-voltage (I-V) characteristics of these devices in the dark and under simulated AM1.5 test conditions are plotted in Figure 2a and Figure 2b, respectively, and the photovoltaic parameters of merit are summarized in Table 1. We note that the air annealing procedure leads to a substantial increase in both the V_{OC} and the FF. Nitrogen annealing had no such positive effect, suggesting that the enhancement of the device performance is related to an oxygen-induced reaction in air.

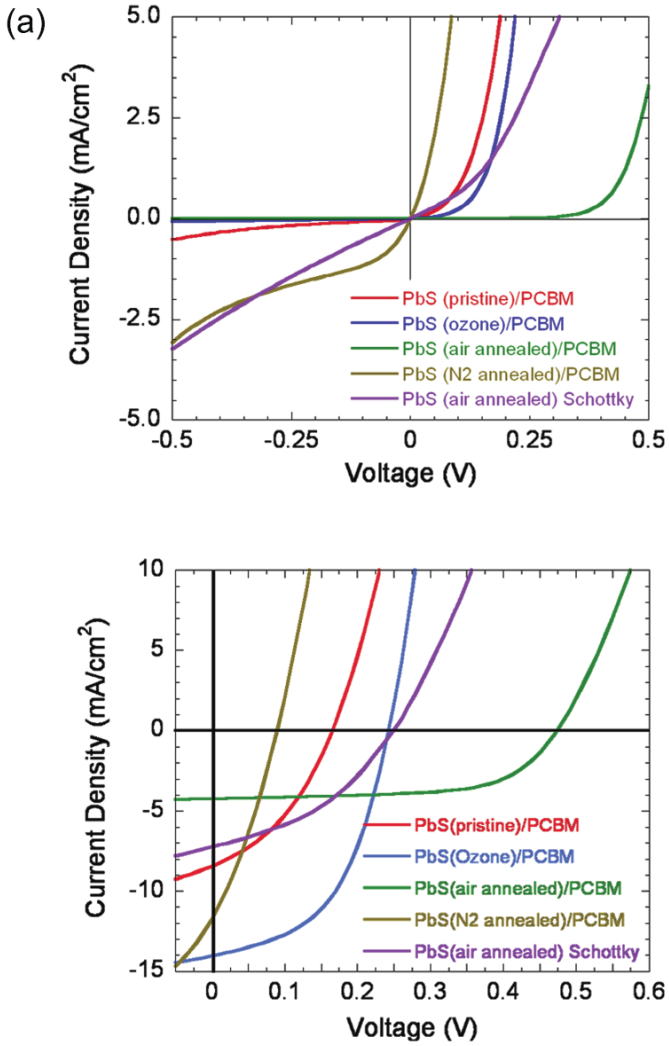

Figure 2. Current-voltage characteristics of representative solar cells (a) in the dark and (b) under 100 mW/cm^2 AM1.5 illumination.

TABLE 1. Response of PbS QD/PCBM Solar Cells under Simulated AM1.5 (100 mW/cm^2) Illumination[a]

PbS QD PVs	J_{SC} (mA/cm^2)	V_{OC} (V)	FF (%)	PCE (%)	R_S (Ω cm^2)	R_{SH} (Ω cm^2)
N_2-annealed	11.7	0.085	32	0.32	1.5	40
pristine	8.2	0.16	38	0.50	2.1	530
ozone-treated	14.0	0.24	50	1.68	1.7	3200
air-annealed	4.2	0.47	62	1.27	16.4	120000
Schottky (air-annealed)	7.2	0.25	38	0.68	20	180

Table 1. Response of PbS QD/PCBM solar cells under simulated AM1.5 (100 mW/cm^2) illumination. The devices are listed in the order of increasing V_{OC} and FF. Response of the Schottky PbS QD/Mg solar cells is also indicated. The series (R_S) and shunt resistance (R_{SH}) are calculated from $\partial V/\partial J$ at V = 0.5V and V = -0.1V~0 V, respectively, for each J-V curve of devices in the dark.

In addition to air annealing, ozone treatment of as-deposited QD films also enhances the V_{OC} and FF. The increase in the photocurrent of the device after the ozone treatment leads to the highest power conversion efficiency among all of the devices studied here. Compared to air annealing, in which samples are subjected to an elevated temperature for 30 minutes, a short room-temperature treatment in ozone (6 seconds long) allows for a rapid surface oxidation process that should facilitate removal of QD capping ligands and formation of an oxide shell for QDs, particularly those at the top surface of the QD film, which form a heterojunction with the PCBM overlayer. Longer ozone exposure results in a decreased J_{SC} and an increased V_{OC}. In the analysis that follows we largely focus on the differences between the pristine and the air annealed bilayer devices as the latter exhibit the highest V_{OC} and fill factor, and contain a more uniformly oxidized QD film as compared to ozone treated devices.

Composition Change during Air Annealing

In order to investigate changes in the chemical composition of the PbS QD films, X-ray photoelectron spectroscopy (XPS) was carried out on the pristine film and on the air annealed films before and after post-annealing EDT treatment. The XPS spectra show the presence of Pb, S, C and O. The atomic ratios of these elements in different samples are summarized in Table 2. As expected, air annealing increases the concentration of oxygen. Following the post-annealing EDT treatment, the oxygen concentration is observed to decrease. Concentrations of Carbon and Sulfur, on the other hand, are observed to increase. To more precisely identify the species formed during the chemical treatments, we focused on the XPS spectra of S 2p and O 1s peaks (Figure 3). Peak fitting of line-shapes to the spectra reveals the presence of PbO, $PbSO_3$ and $PbSO_4$ in PbS QD films after air annealing. Post-annealing EDT treatment reduces the amount of these oxide compounds and changes their relative composition. For instance, the molar ratio between $PbSO_3$ and $PbSO_4$ changes from 1:1.3 to 1:0.7, suggesting a greater reduction in the $PbSO_4$ composition after EDT treatment. This agrees with the earlier study by Konstantatos et al. [28], which showed that thiol treatment can remove the $PbSO_4$ on the surface of QDs while leaving behind $PbSO_3$. As noted earlier, our annealing condition leads to a relatively aggressive oxidation process. Rather than only modifying the surface chemistry of the QDs, as in the case of a solution-phase treatment [28] or short air annealing process [24], it converts a considerable amount of PbS (~40%) to amorphous oxide compounds that surround the QDs. The benefits of creating this morphology will be discussed later. Besides modifying the composition of the oxide compounds, the post-annealing EDT treatment also increases the relative concentration of C-S (thiol) species, indicative of surface trap passivation by EDT ligands. Henceforth, a post-annealing EDT treatment is implied for devices described as having been "air annealed" or "N_2 annealed," unless otherwise specified.

TABLE 2. XPS Chemical Composition (atom %) of the PbS QD Films

films	Pb	S	C	O
pristine	34.7	33.6	30.2	1.5
air-annealed (without EDT)	23.1	19.3	29.8	27.8
air-annealed (with EDT)	21.9	25.7	35.6	16.8

Table 2. XPS chemical composition (atom %) of the PbS QD films. The "with EDT" and "without EDT" refer to with and without post-annealing EDT treatment, respectively.

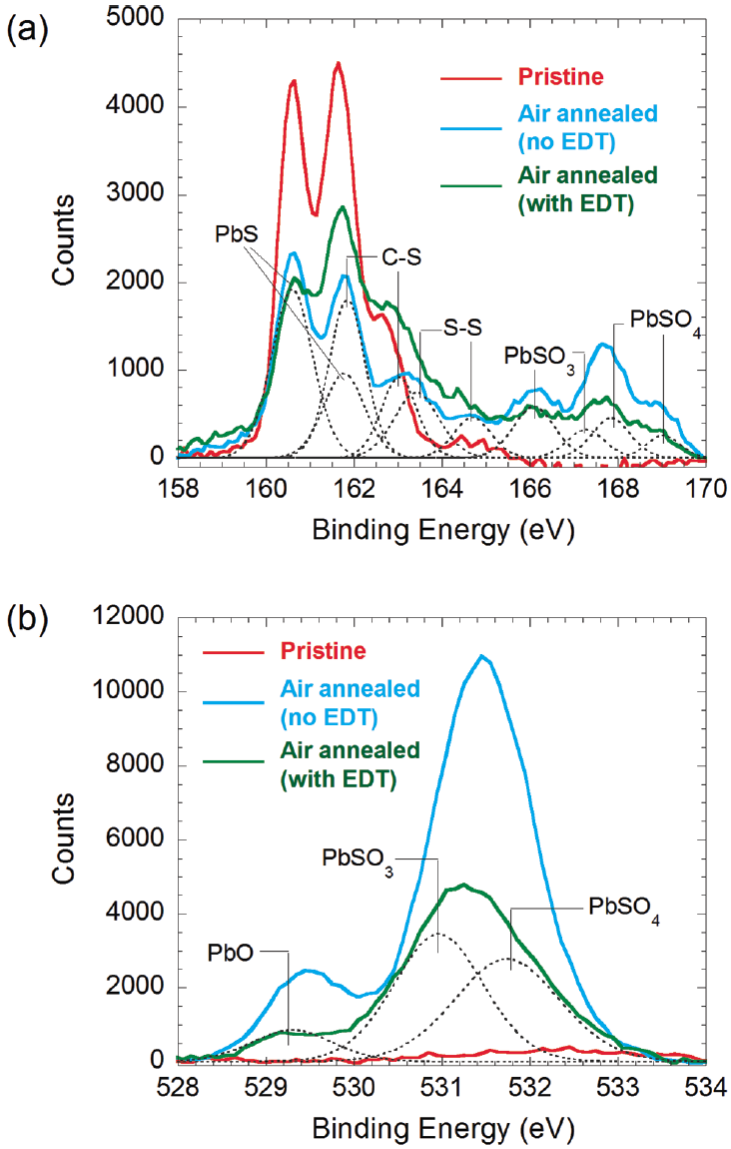

Figure 3. XPS spectra of S 2p (a) and O 1s (b) peaks in pristine (red) QD film and air annealed QD films with (green) and without (cyan) EDT post-annealing treatment. Sulfur species are fitted with a S 2p doublet (dotted line) with 2:1 intensity ratio and 1.18 eV splitting energy. The binding energies for the species are 160.6 eV and 161.78 eV for PbS, 161.85 eV and 163.03 eV for C-S, 163.43 eV and 164.61 eV for S, 166.10 eV and 167.28 eV for $PbSO_3$, and 167.84 eV and 169.02 eV for $PbSO_4$. Oxygen species are fitted with an O 1s singlet (dotted line). The binding energies for the species are 529.3 eV for PbO, 530.96 eV for $PbSO_3$, and 531.7 eV for $PbSO_4$.

Absorption Spectra of QD Films

Changes in the structure of the PbS QD films upon ozone, air and nitrogen treatments are readily observed in their optical absorption spectra (Figure 4a). The pristine film and the ozone treated film show nearly identical absorption features, suggesting that the brief ozone treatment only oxidizes a very small portion of the QDs (presumably those near the film surface) and that the light absorption in the film is dominated by the unoxidized QDs. During air-annealing the

surface of the PbS QDs reacts with oxygen to form oxide compounds as shown in the XPS measurement. The oxide compounds remain as an amorphous matrix around the QDs (as indicated in the band-structure diagram of Figure 1b), while the effective size of the QDs becomes smaller. For our QD films, the spectrum of the air-annealed film exhibits the first excitonic transition at λ=1280 nm, about 170 nm blue-shifted from the corresponding absorption peak of the pristine film, which indicates a 0.1eV increase in the bandgap of the air annealed QDs. This corresponds to a reduction of 0.8 nm in QD diameter, which is consistent with the value extracted from x-ray diffraction data of the films. According to the QD size-dependence of V_{OC} reported in other publications[15, 20, 21], such QD size reduction can lead to 0.05V increase in the V_{OC}, which is insufficient to explain the larger increase (0.3V) in V_{OC} that we observe after air annealing of pristine QD films (See Table I and Figure 2b). For comparison, the absorption spectrum of the nitrogen-annealed film is also plotted in Figure 4a, which, in contrast, has its first excitonic peak slightly red-shifted relative to the peak of the pristine film. This is consistent with a densification of QD films as the nitrogen-anneal introduces slight sintering and causes a solvatochromic effect[29], both of which would lead to the observed absorption red-shift.

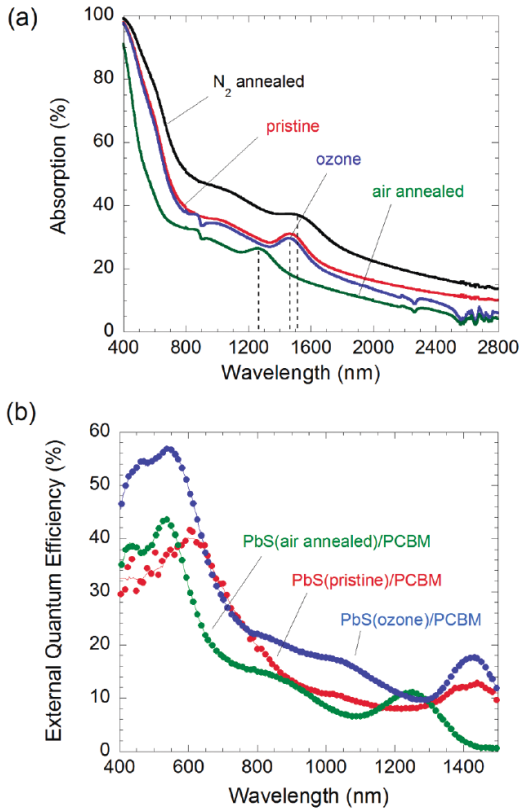

Figure 4. (a) Optical absorption spectra of discrete PbS QD films under different processing conditions. (b) External quantum efficiency (EQE) spectra of PbS QD /PCBM devices.

Besides the shift in the first excitonic transition peak, the total light absorption of the PbS QD film is also reduced after air annealing, due to part of the PbS reacting with oxygen to form wider band gap oxides, which lowers the concentration of the optically absorptive PbS. Figure 4b shows the external quantum efficiency (EQE) of the pristine, air-annealed and ozone-treated devices as a function of wavelength, showing a diminished photoresponse intensity in the air-

annealed devices, reflecting the lower absorption fraction for these structures, as measured in Figure 4a.

Shunt and Series Resistance

Differences in the performance of the devices can be analyzed using a standard equivalent-circuit model (inset in Figure 5), from which we extract the series resistance (R_S) and the shunt resistance (R_{SH}) of each device in the dark (values tabulated in Table I). We note a strong correlation between the V_{OC} and FF and the shunt resistance R_{SH} (Figure 5), with V_{OC} and FF of a device increasing for larger R_{SH}. The finite value of R_{SH} reflects the presence of current leakage paths through the solar cells and/or bimolecular recombination of charge carriers within the solar cells. The air annealing process can efficiently enhance R_{SH} as it can not only form an insulating matrix surrounding the QDs that reduces the leakage current but also provide an energy barrier that suppresses the bimolecular recombination process (Figure 1b).

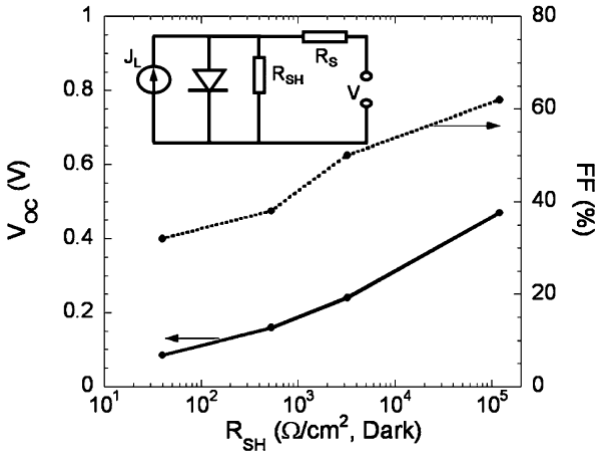

Figure 5. Open circuit voltage (V_{OC}, solid line) and Fill Factor (FF, dashed line) plotted against the derived values of shunt resistance R_{SH}, Inset: Equivalent circuit model of a solar cell.

In contrast to R_{SH}, the variation in R_S among the tested devices is relatively small between the light/dark conditions. R_S is ten-fold higher in the air-annealed devices (both heterostructure and Schottky) as compared to the pristine, nitrogen, or ozone treated solar cells, which reflects the reduction in charge mobility in the air-annealed QD films, due to the oxide growth on the PbS QDs. Although these wide bandgap oxides in PbS QD films lead to a higher R_S, they also increase R_{SH} (Figure 1b), which, in turn, leads to the higher V_{OC} and FF. In contrast, nitrogen-annealed PbS QD films have a low R_S and consequently a higher J_{SC}. However, nitrogen-annealed PbS QDs films fail to produce high a R_{SH}, leading to lower V_{OC} and FF.

Besides R_{SH}, we found that the V_{OC} is also strongly correlated to the turn-on point of the forward current in the dark (Figure 2a). This result is not surprising as V_{OC} corresponds to the situation where the photocurrent is completely balanced by the dark current. Therefore for a fixed photocurrent a late turn-on of the device in the dark will lead to a high V_{OC}. In our devices, the turn-on occurs when recombination of injected electrons and holes prevails in the forward bias. Hence a device with diminished charge recombination rate (i.e. device that can build-up a larger quantity of separated charges) would yield a high V_{OC}.

Comparing Bilayer and Schottky Solar Cells

The benefit of incorporating a PCBM layer into the photovoltaic structure is evident from the comparison of the air-annealed PbS QD/PCBM bilayer device with a Schottky solar cell consisting of just the air-annealed PbS QD layer in direct contact with the Mg/Ag cathode. The R_S for both structures is nearly the same, indicating that the PCBM film does not dominantly contribute to the series resistance of these cells. The V_{OC} and FF are higher in the bilayer device, reflecting a higher charge build-up and smaller leakage. The Schottky device, however, exhibits a larger short-circuit current (J_{SC}), which can result from a wider depletion region for exciton dissociation[15, 17] and/or a higher efficacy of exciton dissociation at the QD/cathode interface due to the reduced charge build-up. It is also notable that in our experiments the device yield and reproducibility are much higher in the bilayer device structure, presumably due to the PCBM layer effectively blocking metal penetration through the QD layer during the evaporation of the top electrode, reducing leakage paths and yielding a more reproducible electron transfer interface.

The effect of bimolecular recombination on V_{OC} can also be seen by comparing the performances of the pristine bilayer device and the air annealed Schottky device: The former has a lower leakage current (as shown in Figure 2a) and a higher R_{SH}, however its V_{OC} is lower than the air annealed Schottky device. This suggests that reducing the leakage current alone is not sufficient to achieve a high V_{OC} and that suppression of charge recombination is vital in the bilayer devices.

Light Intensity Dependence and Charge Transport

The current-voltage characteristics of the devices were measured under monochromatic infrared (IR) light illumination (λ=1310 nm) of different intensities, where PCBM is transparent for the selected wavelength of IR light, ensuring that all of the photogeneration is taking place in the PbS QD film. We observe that the high V_{OC} and FF are maintained in the IR-illuminated air-annealed devices (Figure 6a), and that the IR power conversion efficiency reaches 2.4%. This not only confirms that the shape of the *I-V* characteristics is determined by the PbS QD layer but also proves that such devices can be used to efficiently harvest the IR portion of sunlight.

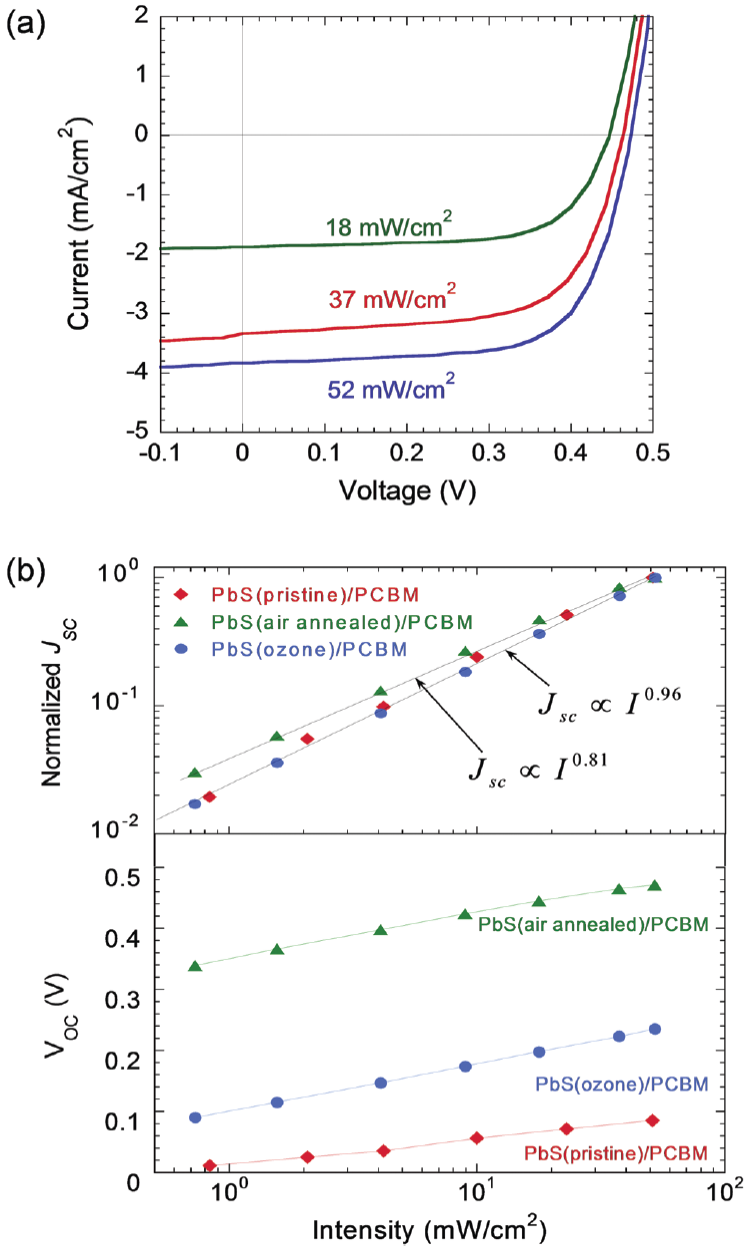

Figure 6. (a) Current-voltage characteristics of an air annealed device under monochromatic IR illumination (λ = 1310nm) at different intensities. (b) (Top) Incident light intensity dependence of the normalized short-circuit current (J_{SC}) for PbS QD /PCBM devices. The experimental data (symbols) are fitted (solid lines) using . (Bottom) Incident light intensity dependence of the open-circuit voltage (V_{OC}).

The light intensity dependence of the normalized short-circuit current density (J_{SC}) under IR illumination is plotted in Figure 6b for the pristine, air-annealed, and ozone-treated devices. The experimental data are fitted with $J_{sc} \propto I^{\alpha}$ to ascertain the contribution of charge recombination in the loss mechanism for the photocurrent. It has been predicted that α=1 when the photocurrent is determined by the generation rate of electron-hole pairs upon photon absorption; while α=0.75 when the photocurrent is further limited by formation of space-charge regions due to unbalanced charge transport for electron and holes[30]. In our experiment α=0.96 for

the pristine and ozone treated device and α=0.81 for the air annealed device, suggesting that the air annealing treatment and subsequent post-annealing thiol treatment limit the charge transport properties of the PbS QD film, leading to a space-charge effect. To elucidate this point, we measured charge transport through the PbS QD films in a field-effect transistor (FET) geometry in the linear regime and found that the hole mobility in the QD film decreases from $5.0x10^{-3}$ $cm^2/(Vs)$ to $5.5x10^{-5}$ $cm^2/(Vs)$ after air annealing/thiol post-annealing treatment. The decrease in the film mobility can again be attributed to the insulating oxide compounds acting as a barrier for charge transport. The fact that the fill factor increases after air annealing shows that the bias dependence of the photocurrent is much less affected by the reduced charge transport than it is by the increased shunt resistance, which would suggest that the initial geminate pair separation is very efficient in the QD films.

Figure 6b also shows the increase in V_{OC} for the three types of devices with the increasing IR-light intensity. The increase of V_{OC} with intensity is the largest for the air-annealed devices, which can be attributed to a low recombination rate of the photogenerated charges in these structures. In contrast, faster recombination in the pristine PbS QD films leads to rapid depletion of the separated photogenerated charge and hence a lower increase of the V_{OC} with light intensity. The ozone-treated devices represent an intermediate situation. It is likely that in these devices only the interface QDs are oxidized. Therefore the increase in their V_{OC} values, as compared to the pristine-devices, would originate from the reduced charge recombination at the QD/PCBM heterointerface; while the decrease of the V_{OC} in the ozone treated devices, as compared to the air annealed devices, reflects the fast charge recombination in the unoxidized bulk QD films. The direct measurement of the charge recombination rates for different structures is discussed in the next section.

Charge Carrier Recombination Lifetime

To directly measure charge recombination in the PbS QD/PCBM bilayer solar cells, we performed small perturbation transient open-circuit voltage decay measurements[31-33]. In this measurement, a DC biased IR light source (λ=1310 nm) is used to illuminate the device to create excitons that dissociate into electrons and holes. The separated carriers fill up the sub-band gap states between the conduction and valence band edges and increase the distance between the quasi-Fermi levels for electrons and holes, E_{Fn} and E_{Fp}, respectively. In an open-circuit condition, this is manifested as the measured V_{OC}. Simultaneously, a low-intensity pulsed IR light is used to induce a small perturbation to the V_{OC} by transiently generating additional electrons and holes. This leads to a small and momentary increase in the energy difference between E_{Fn} and E_{Fp}. The resulting additional transient photovoltage, ΔV, will then decay with a lifetime τ that is determined by the recombination rate constant (k_{rec}, $\tau = 1/ k_{rec}$) of the electrons and holes. Figure 7a shows the transient voltage decay curves of pristine and air annealed devices, which can both be fitted to a monoexponential decay function to extract the lifetime τ and consequently the k_{rec}.

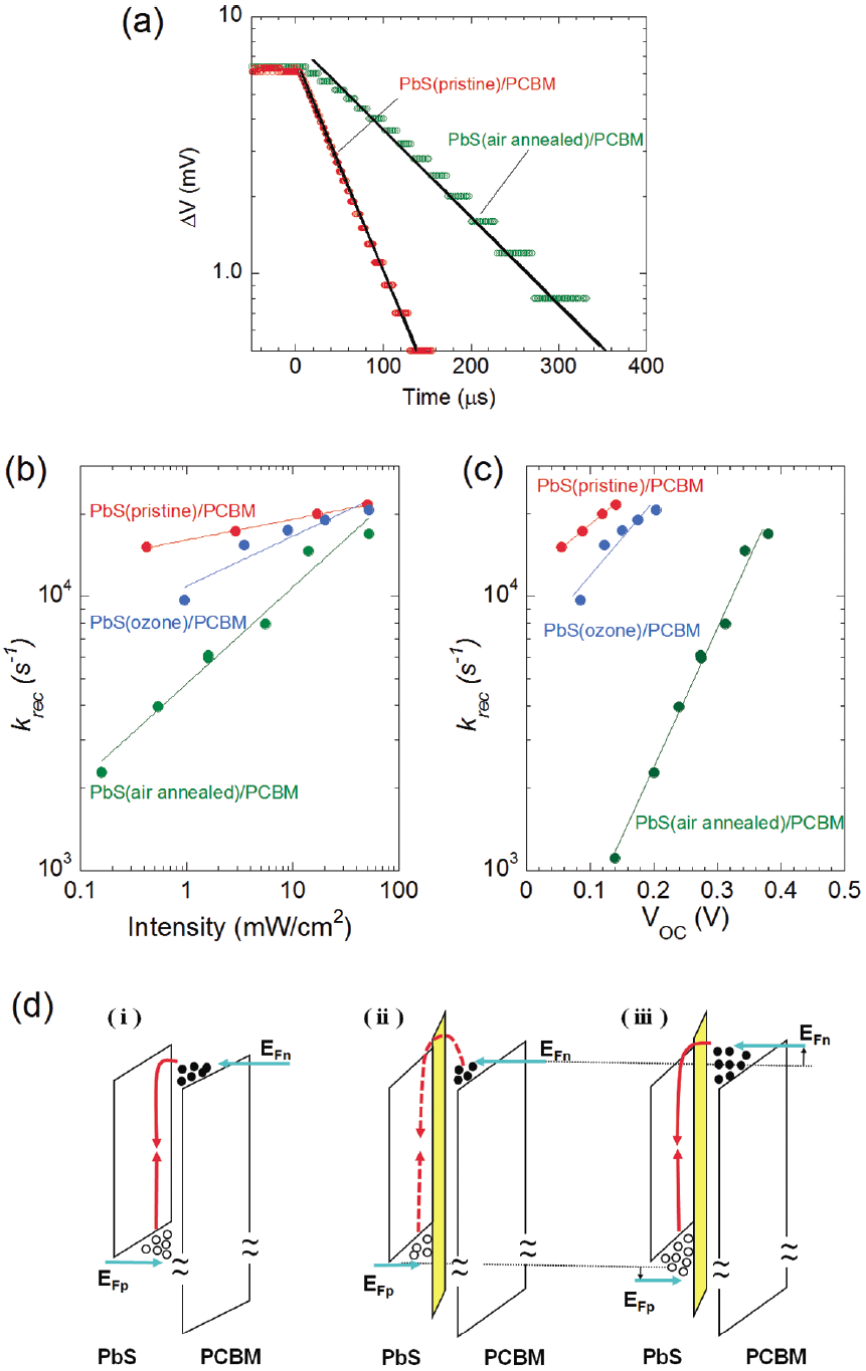

Figure 7. (a) Typical transient photovoltage (ΔV) decay data together with a monoexponential decay function fit at 0.5 mW/cm^2. (b) k_{rec} vs light intensity and (c) k_{rec} vs V_{OC} measured for the pristine, ozone-treated and air-annealed devices. (d) Charge recombination process in the devices at an open-circuit condition for a pristine device (i), and an air-annealed device at low light intensity (ii) and at high light intensity (iii). The red arrows denote charge recombination process, with the solid and dashed lines indicating fast and slow recombination rates, respectively. Note that the mechanism also applies to the bulk PbS QD layer between a QD donor and a QD acceptor.

In Figure 7b we plot k_{rec} as a function of the DC biased light intensity. For all the devices k_{rec} increases with increasing light intensity. This is expected as the mobility of charge carriers is improved as more traps become filled by photogenerated charge carriers and the improved mobility can consequently increase the charge recombination rate constant by increasing the frequency of opposite charge carriers encountering each other. We observe that the air-annealed device exhibits a k_{rec} much smaller than the pristine and ozone-treated device at low light intensities, indicating that at low photogenerated charge carrier concentrations the charge loss due to recombination process is greatly suppressed in the air-annealed device. The reduced charge loss compensates the reduction of photogenerated carriers at low light intensities, which explains the maintaining of high V_{OC} in the air-annealed device at such conditions. The correlation of k_{rec} and V_{OC} is plotted in Figure 7c. For the pristine devices, even at low V_{OC} k_{rec} is relatively large, hampering a steady-state accumulation of separated photogenerated charge. For the air-annealed devices a similarly high k_{rec} is only observed at much larger values of V_{OC} when a significant amount of photogenerated charge is separated.

Based on the above observations we propose a model (Figure 7d) to explain the charge recombination process in our devices at an open-circuit condition. In the air annealed device a thin layer of oxide compounds at the PbS QD/PCBM interface can act as a barrier for charge recombination. At low light intensities there is only a small amount of photogenerated carriers available to fill up the sub-gap states. Therefore, the position of the electron Fermi level is low and the activation energy required for charge carrier recombination is high, resulting in a low k_{rec}. As the light intensity increases more sub-gap states are filled with photogenerated electrons, which further raises the electron Fermi level and accelerates the charge recombination process until eventually, the electron transfer from the PbS QD to PCBM is matched by the back electron transfer, thus pinning the photovoltage. In this situation the V_{OC} saturates and the k_{rec} probed by the transient V_{OC} measurement reflects the recombination rate constant within the QD film. For the pristine device since there is minimal oxide barrier at the PbS QD/PCBM interface the charge recombination can occur relatively easily even at low light intensities and the electron Fermi level can only move a small amount before the back electron transfer limits the photogeneration process, leading to a low maximum V_{OC}.

It is important to note that the suppression of bimolecular recombination that results from air annealing occurs not only at the PbS QD/PCBM interface but also between QDs in the bulk PbS QD film. It has been shown that due to the high dielectric constant of PbS, a wide depletion region (~150nm) can form in the PbS QD film of a Schottky solar cell structure under short-circuit conditions. In our bilayer devices, the width of this depletion region will be reduced due to insertion of the PCBM layer, although it may still significantly contribute to the photocurrent. Therefore, at voltages lower than the open-circuit voltage, i.e. before the depletion region width reaches zero, bimolecular recombination of charge carriers between QDs must also be taken into consideration in modeling of the electronic processes that govern device operation.

Conclusion

We fabricated PbS QD-based solar cells that incorporate PCBM as the electron transporting/hole blocking layer. By applying a simple two-step processing method consisting of air annealing and a post-annealing thiol treatment we are able to modify the surface properties of the PbS QDs and consequently the performance of the solar cells. We show that the fill factor of

the device is predominantly affected by the shunt resistance of the device, which can be enhanced by (1) using a bilayer structure and (2) creating a film morphology where QDs are surrounded by the less conductive oxide compounds that spatially separate photogenerated charges, inhibiting their recombination, and leading to increased V_{OC}. Presently, the power conversion efficiency of the air-annealed devices is limited by the low photocurrent, which is largely due to the low optical absorption and the high series resistance of the QD films. The field dependence of the photocurrent in these structures appears to be dominated by charge transfer and charge recombination processes and is less affected by charge transport. These insights demonstrate the importance of limiting current leakage and interfacial charge recombination in QD solar cells (which is reflected in the high shunt resistance and late turn-on in the forward bias) and suggest that introduction of an inert interfacial layer (such as that of PbO on PbS QDs) can assist in maintaining the high V_{OC} and FF.

2. Improved Current Extraction from ZnO/PbS Quantum Dot Heterojunction Photovoltaics Using a MoO_3 Interfacial Layer

Among the variety of device architectures explored for PbS QD-based solar cells, oxide/QD *np* heterojunctions have shown particular promise, with NREL-certified efficiencies of 3% and lifetimes in excess of 1000 hours reported for ZnO/PbS.[34] Efficiencies of 5.1% and 8% at room temperature[35] and 170 K,[36] respectively, have also been reported for TiO_2/PbS, which suggests that the efficiency limits may be much higher. These oxide/QD heterojunctions have the advantage of positioning the illuminated optical field maximum within the depleted region of the QD film, enabling high carrier collection efficiency while still allowing for thick, highly absorptive films. In QD Schottky solar cells, on the other hand, the depleted region is located at the rear QD/metal contact, which necessitates the use of thinner active layers to ensure that the maximum number of photons is absorbed within the depleted region. Due to the inverted architecture of the oxide/PbS *np* heterojunction, a high-work function electrode is desirable for the top contact to reduce the presence of a Schottky barrier impeding the extraction of holes from the *p*-type PbS active layer.[37,38] However, Gao and Luther have shown that Fermi-level pinning can lead to the formation of a Schottky barrier even between PbS and gold, despite the close alignment between the Fermi level of gold and the valence band edge of PbS.[38,39] Similar back-contact Schottky barriers have also been noted in CdTe thin-film solar cells,[40] and lead to sizeable reductions in the open circuit voltage, fill factor, and efficiency.

Here, it is demonstrated that the insertion of a thin film of molybdenum oxide (MoO_3) between the PbS photo-active layer and the anode contact inhibits the formation of a Schottky junction. Molybdenum oxide has previously been utilized as a hole-injection layer for organic thin films,[41,42] as both an electron-blocking layer and a physical buffer layer in photovoltaics,[43-49] and as a charge-transfer dopant in organic FETs.[50] In the architecture described here, the high work function of MoO_3 is found to pin the Fermi level of the top electrode, enabling the formation of an ohmic contact to PbS and allowing even low-work function metals to be used as the anode without forming a voltage-limiting Schottky contact. The MoO_3 thus allows the performance of the device to be effectively decoupled from the properties of the anode material, which enables the use of a transparent ITO anode to optically probe different interfaces within the device and potentially to facilitate the design of stacked multijunction devices. We demonstrate that the removal of this opposing Schottky diode barrier in ZnO/PbS heterojunctions

leads to an enhancement in the short-circuit current (J_{SC}), open-circuit voltage (V_{OC}), and fill factor (FF) of the device, resulting in a power conversion efficiency (η_P) of 3.5 ± 0.4% under AM1.5G illumination.

ZnO/PbS Heterojunction

Figure 8 shows the flat-band energy level diagram of the device, with energy values taken from the literature[51-53]. The inclusion of the MoO_3 interlayer in the device structure strongly influences the *J-V* characteristics, as shown in Figure 9 for a series of devices with an ITO anode, all illuminated from the ZnO side. For the device without MoO_3, a "roll-over" in the forward-bias photocurrent ($V > 0.5$ V) is observed, similar to that reported by Gao *et al.* for ZnO/PbS heterojunction devices employing a silver anode[38] and by Lin *et al.* for CdS/CdTe/Ni devices.[54] The roll-over is consistent with the presence of a Schottky barrier at the PbS/anode contact in opposition to the *np* heterojunction diode formed at the ZnO/PbS interface. Such a Schottky barrier would impede the extraction of holes from the PbS active layer, limiting both the dark current and the photocurrent in forward bias and reducing the V_{OC}, as is observed in Figure 9. The incorporation of MoO_3 between the PbS and the top ITO contact reduces this roll-over effect, simultaneously increasing the J_{SC}, V_{OC}, and FF of the device and resulting in up to a 4.5-fold increase in the power conversion efficiency, from η_P = 0.64% without MoO_3 (J_{SC} = 7.2 mA cm^{-2}, V_{OC} = 0.31 V, and FF = 0.29) to η_P = 2.9% with a MoO_3 thickness of 50 nm (J_{SC} = 14.6 mA cm^{-2}, V_{OC} = 0.58 V, and FF = 0.35).

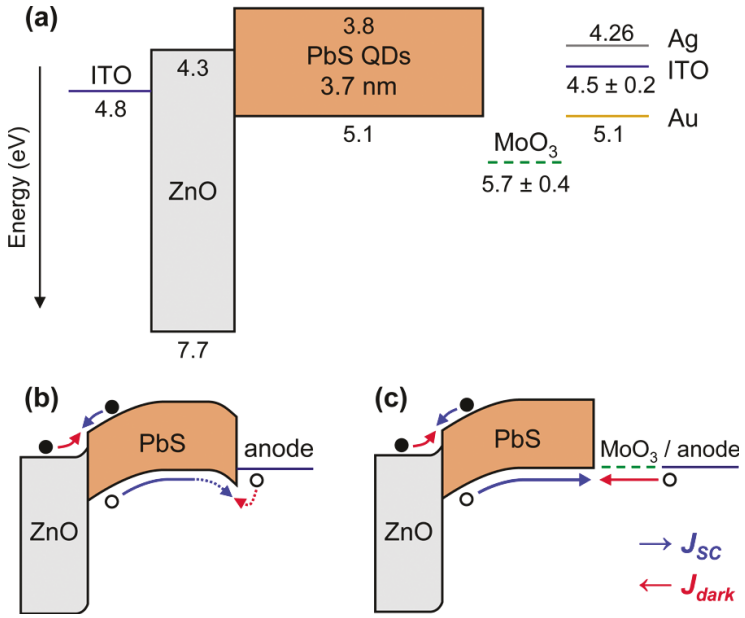

Figure 8. (a) Flat-band energy level alignment of the thin films constituting the ZnO/PbS heterojunction photovoltaic device. Band energies are given in eV and are taken from literature. Illumination under normal operation is incident from the ZnO side. (b) Proposed band-bending in the MoO_3-free device, showing the depleted *np* heterojunction at the ZnO/PbS interface and a hole-current-limiting Schottky contact at the PbS/anode interface, and (c) the removal of the Schottky contact following the insertion of MoO_3 between PbS and the anode material.

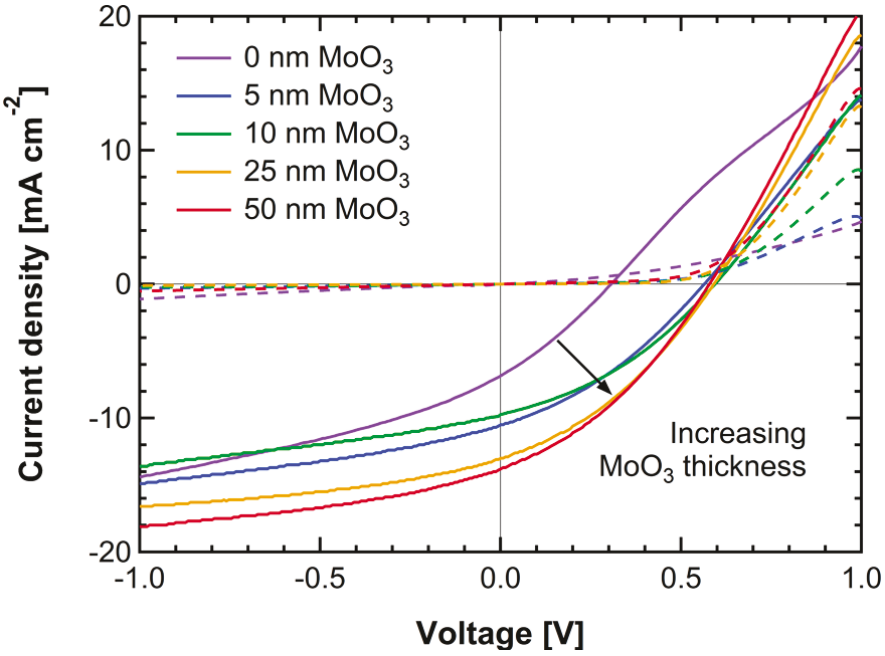

Figure 9. *J-V* characteristics measured in the dark (dashed lines) and under 100 ± 10 mW cm^{-2} AM1.5G illumination (solid lines) for ITO/ZnO/PbS/MoO_3/ITO devices with varying thicknesses of MoO_3. Each curve represents the average of seven to ten devices fabricated on the same substrate. The roll-over in light current observed at +0.5 V for the device without MoO_3 is ascribed to the presence of a Schottky junction at the anode contact. The addition of MoO_3 alleviates this roll-over and simultaneously increases the J_{SC}, V_{OC}, FF, and η_P.

The effects of the MoO_3 interlayer are also discernable in the dark *J-V* characteristics. In Figure 10, the dark current for a range of MoO_3 thicknesses is plotted along with its fit to the generalized single-diode Shockley equation[55]

$$J = \frac{R_p}{R_s + R_p}\left\{J_S\left[\exp\left(\frac{e(V - JR_s)}{nk_BT}\right) - 1\right] + \frac{V}{R_p}\right\} \quad (1)$$

where R_p is the shunt resistance, R_s is the series resistance, J_S is the reverse saturation current, and n is the diode ideality factor. An improved fit to the measured *J-V* data is observed for increasing MoO_3 thickness, corresponding to the removal of the Schottky diode at the PbS/anode interface, which is not accounted for by the single-diode equation. A diode ideality factor of n = 2.0 ± 0.1 for a MoO_3 thickness of 50 nm indicates that the *J-V* behavior of this device is indeed consistent with the single-diode. An increase in the forward-bias dark current is also observed, which reflects the increased hole extraction efficiency brought about by the reduction in the Schottky barrier height. This effect is consistent with reports of enhanced hole injection into organic hole-transport layers upon insertion of a MoO_3 interlayer between the active organic layer and an ITO anode.[41]

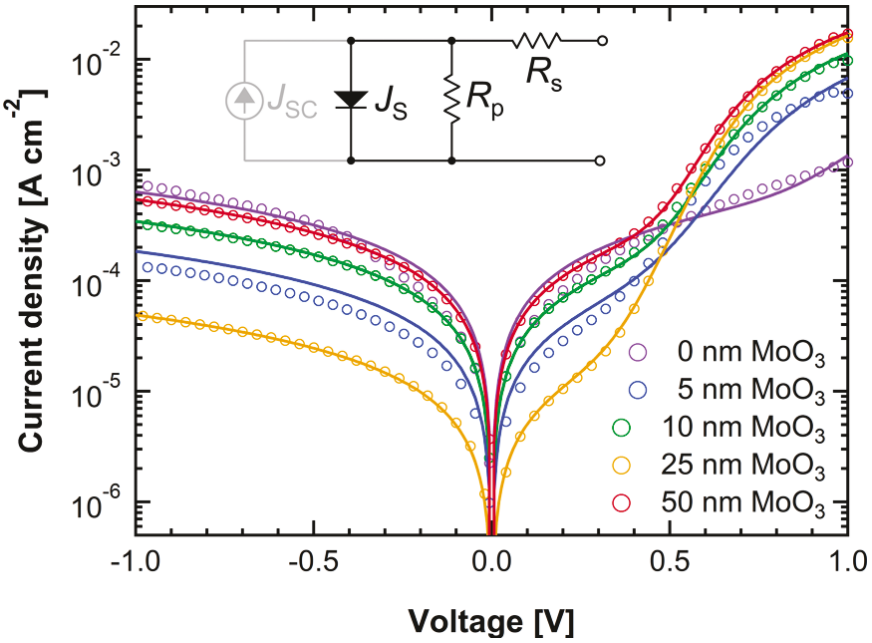

Figure 10. Dark current for representative ITO/ZnO/PbS/MoO_3/ITO devices with varying MoO_3 thickness (circles) and fit to the generalized Shockley equation (solid line). The diode fitting parameters R_p, R_s, J_s, and n are defined in the text. The improved fit to the single-diode equation with increasing thickness of MoO_3 reflects the attenuation of the back Schottky diode, and a diode ideality factor of n = 2.0 ± 0.1 for the device employing 50 nm of MoO_3 indicates that the behavior of this device is well-described by a single diode model.

Semi-Transparent Schottky Device

The roll-over behavior and interfacial energy level alignment are further explored by removing the *n*-type ZnO layer. In this case, the characteristics of the PbS/anode and PbS/MoO_3 interfaces may be probed without interference from the *np* heterojunction diode at the ZnO/PbS interface. Figure 11 compares the *J-V* characteristics of a glass/ITO_P/PbS/ITO device and a device employing a 5 nm thick interlayer of MoO_3 between PbS and the top ITO electrode (glass/ITO_P/PbS/MoO_3(5 nm)/ITO); ITO_P refers to annealed, O_2 plasma-cleaned ITO, which is expected to form a low-injection-barrier contact to PbS.[56] In-situ sputtered ITO is known to have a lower work function than O_2-plasma-cleaned ITO;[57,58] thus, for a *p*-type PbS QD film, a Schottky junction with downward band-bending is expected to form at the top interface of the glass/ITO_P/PbS/ITO device. Without an *np*-heterojunction at the bottom interface, this Schottky junction dominates the device performance, explaining the reversal of the polarity and direction of rectification relative to the heterojunction devices shown in Figure 9. Upon insertion of MoO_3 between the PbS active layer and the top ITO electrode, a significant change in device operation is observed: the direction of rectification is reversed and the V_{OC} changes polarity, from -0.23 V without MoO_3 to +0.10 V with MoO_3. The reversal of the direction of rectification and, correspondingly, of the built-in potential shows that the effect does not arise from an asymmetric blocking of photogenerated electrons by MoO_3 or a related exciton-blocking effect. The magnitude and direction of the change in V_{OC} in this Schottky device reflects the ~0.3 V increase in V_{OC} upon the inclusion of MoO_3 in the complete ZnO/PbS heterojunction device, providing further evidence for the role of MoO_3 in diminishing the top-contact Schottky barrier.

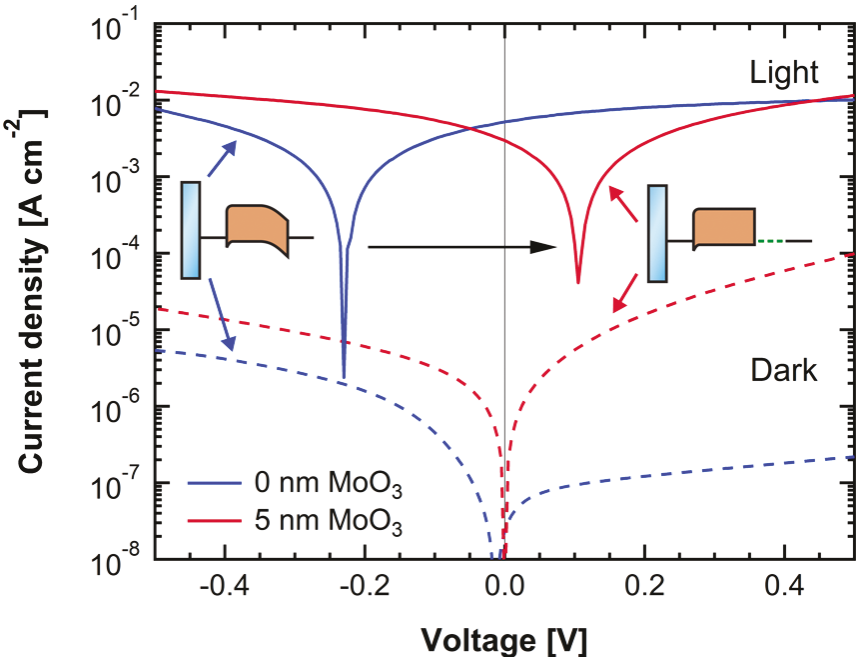

Figure 11. *J-V* characteristics of ITO_P/PbS/ITO and ITO_P/PbS/MoO_3(5 nm)/ITO devices in light (solid curves) and dark (dashed curves). The insets represent the proposed band-bending in each device. A reversal of the diode rectification ratio in dark, and of the polarity of the V_{OC} and J_{SC} in light, indicates the attenuation of the top Schottky contact upon incorporation of MoO_3.

The use of transparent ITO as the top contact enables illumination of the device from either the bottom ITO_P/PbS interface or the top PbS/MoO_3/ITO interface, which allows for further characterization of the interfacial energetics. In Figure 12, the external quantum efficiency (EQE) spectra of the glass/ITO_P/PbS/ITO and glass/ITO_P/PbS/MoO_3(5 nm)/ITO devices described above are displayed for both bottom-illumination (as in normal device operation) and top-illumination. The absorbance of PbS QDs is stronger in the blue region of the spectrum than in the red; for the 3.7 nm QDs used here, $\alpha^{-1} \sim 55$ nm for wavelength $\lambda = 400$ nm, as compared to $\alpha^{-1} \sim 400$ nm for $\lambda = 600$ nm, where α is the optical absorption constant. Thus, in a spectrally-resolved measurement of the EQE, the blue region of the EQE primarily reflects the current resulting from carrier generation near the illuminated interface, while the red region of the EQE reflects carrier generation throughout the bulk of the active layer.[39,59] A close match between the transmission of the bottom ITO electrode and the top ITO electrode, as well as the high transmission of the 5 nm thick MoO_3 film (>90% for λ >380 nm), indicate that any differences in the EQE spectra can primarily be ascribed to changes in device internal efficiencies rather than optical absorption.

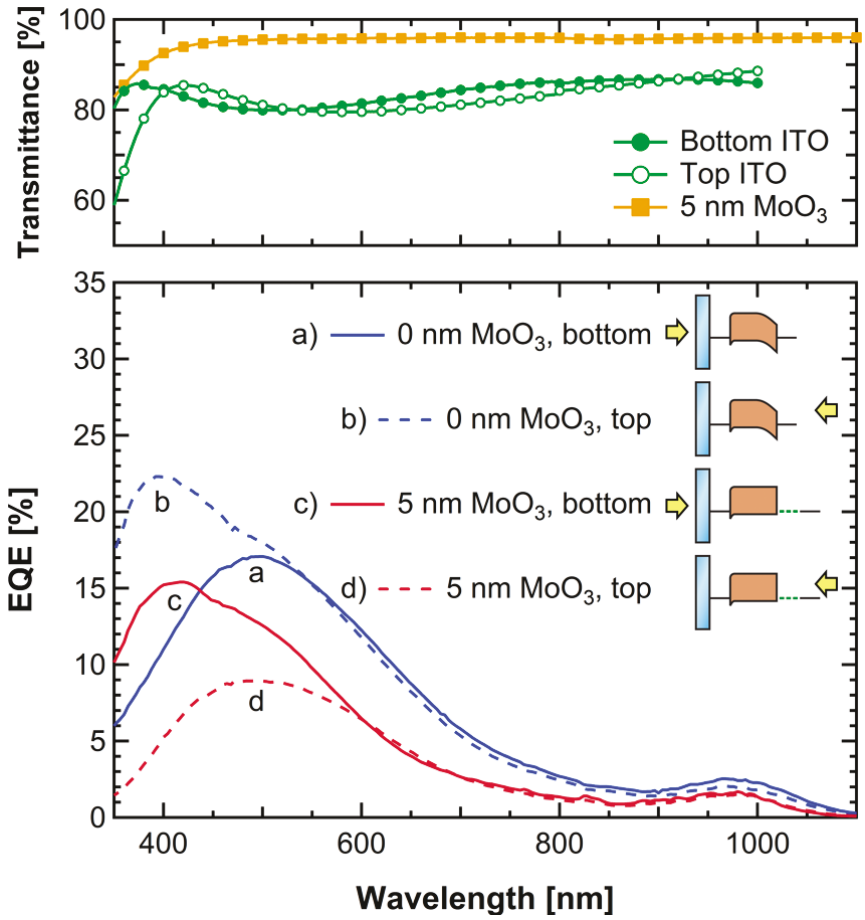

Figure 12. EQE spectra of the ITO_P/PbS/ITO and ITO_P/PbS/MoO_3(5 nm)/ITO devices shown in Figure 11, measured with illumination from the bottom (solid lines), as in normal operation, and from the top (dashed lines). Transmission spectra of the bottom ITO_P, top ITO, and 5 nm MoO_3 layer are included. The inset figures illustrate the proposed change in the spectral response resulting from attenuation of the top Schottky diode by incorporation of MoO_3.

For the device without a MoO_3 interlayer, the EQE peaks at a greater magnitude and lower wavelength for top-illumination ($\lambda_{max,\ top}$ = 392 nm) than for bottom-illumination ($\lambda_{max,\ bottom}$ = 500 nm). This trend supports a more strongly photoactive top section of the device, which is consistent with the identification of a Schottky junction at the top PbS/ITO interface that sweeps electrons to the top ITO electrode and holes to the bottom ITO_P electrode. This polarity is opposite from the intended operation of the complete ZnO/PbS device. In contrast, for the device incorporating a 5 nm MoO_3 interlayer, the EQE peaks at a lower wavelength for bottom-illumination ($\lambda_{max,\ bottom}$ = 420 nm) than for top-illumination ($\lambda_{max,\ top}$ = 496 nm). The four-fold decrease in top-illuminated EQE at λ = 400 nm for the MoO_3-containing device relative to the MoO_3-free device, in conjunction with the polarity reversal of the photocurrent, directly corresponds to the attenuation of the Schottky-junction-induced depletion region at the PbS/anode interface. It also indicates that, while the work function of MoO_3 is greater than the ionization energy of PbS (Figure 8), the MoO_3 does not induce significant upward band-bending at the interface, which would provide an additional driving force for exciton dissociation and

hole collection at the top interface. Instead, the Fermi level of the MoO_3 is likely pinned to that of the PbS, which generates an ohmic contact. A weak downward band-bending at the bottom ITO_P/PbS interface would then explain the greater low-wavelength EQE in bottom illumination than in top illumination for the MoO_3-containing device. We note that in this particular experiment the EQE for the MoO_3-free device corresponds to photocurrent of polarity opposite to that generated at the ZnO/PbS heterojunction, representing a loss mechanism in the complete device. The inversion of polarity and overall decrease in EQE for the device incorporating MoO_3 indicate the attenuation of this loss pathway.

Electrode and Thickness Dependence

While the choice of ITO as the anode material allows optical characterization of the PbS/MoO_3 interfacial energetics and a direct demonstration of the effect of MoO_3 in attenuating the back-contact Schottky barrier, it also introduces transmissive losses for long-wavelength light. Capping the ITO anode with a reflective layer of silver allows for greater optical absorption in a thinner, and correspondingly less resistive, PbS active layer; optical simulations show that for the PbS active layer thicknesses used here, the incorporation of a silver back reflector results in a ~30% increase in the integrated absorption. In Figure 13, the *J-V* characteristics of a complete ITO_P/ZnO/PbS/MoO_3(10 nm)/ITO(100 nm)/Ag heterojunction device are displayed for a range of active layer thicknesses. A linear increase in J_{SC} is observed with increasing PbS thickness up to a PbS thickness of 175 nm. This result is consistent with Mott-Schottky measurements indicating a 200 ± 30 nm depleted region in PbS at the heterojunction interface. For an active layer thickness less than or equal to the depletion width, efficient carrier generation and transport is achieved throughout the entire active layer as a result of the built-in electric field. For PbS thicknesses greater than 175 nm, a rolloff in J_{SC} and a sharp drop in FF is observed, corresponding to a widening of the quasi-neutral region at the rear of the device and a resulting increase in series resistance.

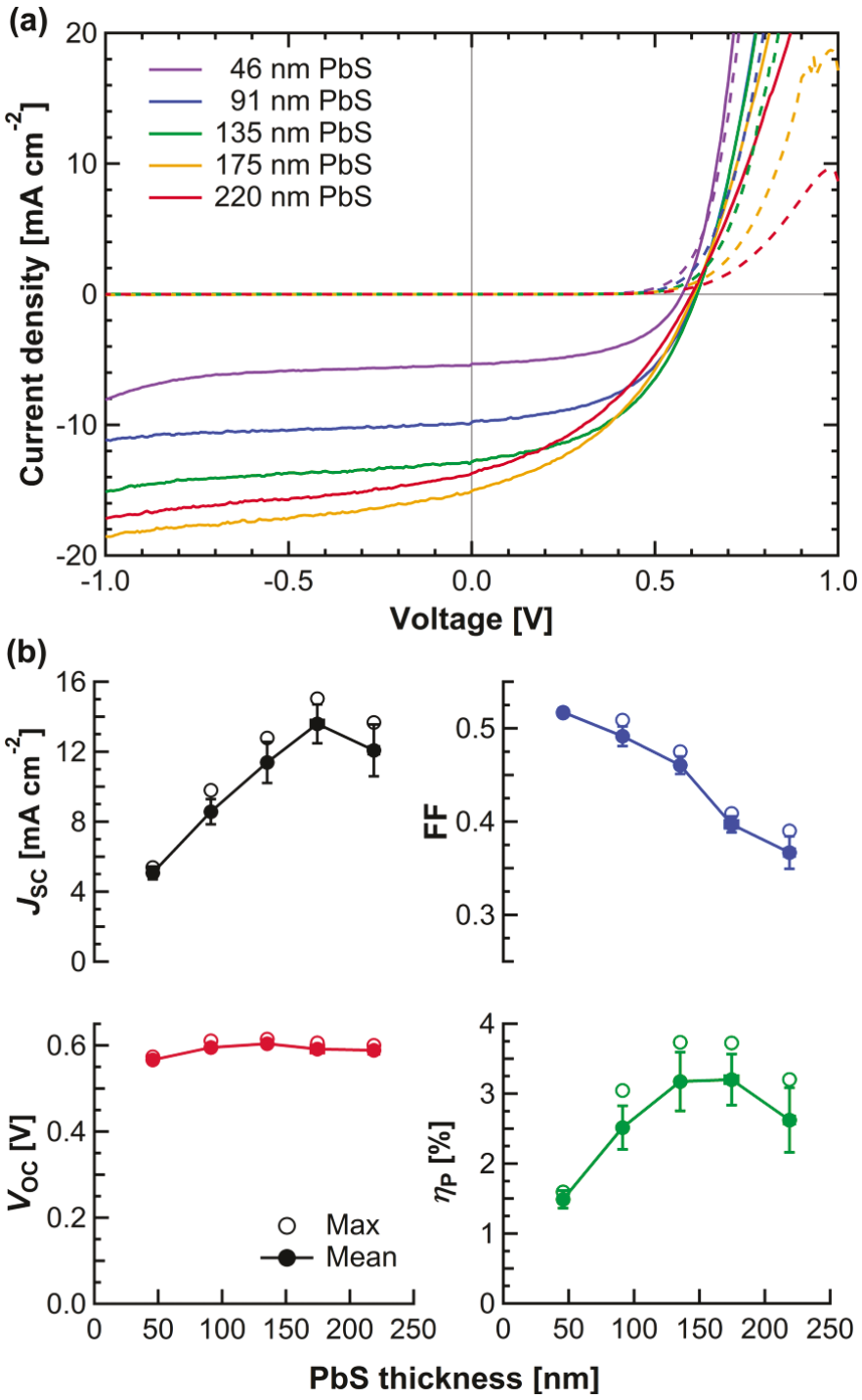

Figure 13. (a) *J-V* characteristics of ITO/ZnO/PbS/MoO_3/ITO/Ag devices employing a 10 nm layer of MoO_3, a 100 nm layer of ITO, and a PbS layer of varying thickness. (b) Performance characteristics of the above devices. Filled circles and error bars correspond to the average and standard deviation across five to six devices on the same substrate, and empty circles represent the value for the best-performing device. Lines serve as a guide to the eye. An efficiency maximum is achieved for a 135 nm-thick PbS layer, with J_{SC} = 11 ± 1 mA cm^{-2}, V_{OC} = 0.60 ± 0.1 V, FF = 0.46 ± 0.01, and η_P = 3.2 ± 0.4%.

Alternatively, the sputtered ITO layer may be omitted, enabling a metallic anode to be evaporated directly onto the PbS/MoO_3 active layer. If MoO_3 does pin the Fermi level of the top electrode material, as suggested by the results described above using an ITO anode, then the V_{OC} would be expected to be independent of the anode work function for devices employing a MoO_3 interlayer. In Figure 14, the *J-V* characteristics of ZnO/PbS heterojunction photovoltaics employing ITO, Ag, and Au anodes with and without a MoO_3 interlayer are displayed. The device performance parameters (J_{SC}, V_{OC}, η_P, FF, R_p, and R_s) are summarized in Figure 15. A convergence of the V_{OC} with increasing MoO_3 thickness is indeed observed, irrespective of the anode material. For devices without a MoO_3 interlayer, the V_{OC} varies with the anode work function in a manner reflecting the presence of a Schottky contact between the *p*-type PbS active layer and the anode, with a lower V_{OC} obtained for lower-work function materials (V_{OC} = 0.29 V for Ag, 0.31 V for ITO, and 0.41 V for Au, which have work functions of 4.3, 4.5±0.2, and 5.1 eV, respectively[57,60]). However, for a sufficiently thick layer of MoO_3, the V_{OC} increases to 0.59 ± 0.01 V for each of the electrode materials, despite a difference of up to 0.8 eV in the electrode work functions. For all three electrodes, an increase in the forward-bias dark current upon the insertion of MoO_3 further reflects the transition from a Schottky contact to an ohmic contact at the PbS/anode interface. The 2.3-fold increase in η_P for the Ag-anode device (η_P = 1.4% without MoO_3 and 3.1% with 25 nm thick MoO_3) and 1.5-fold increase for the Au-anode device (η_P = 2.3% without MoO_3 and 3.5% with 5 nm thick MoO_3) demonstrate the dramatic effect of this improved contact on the device performance.

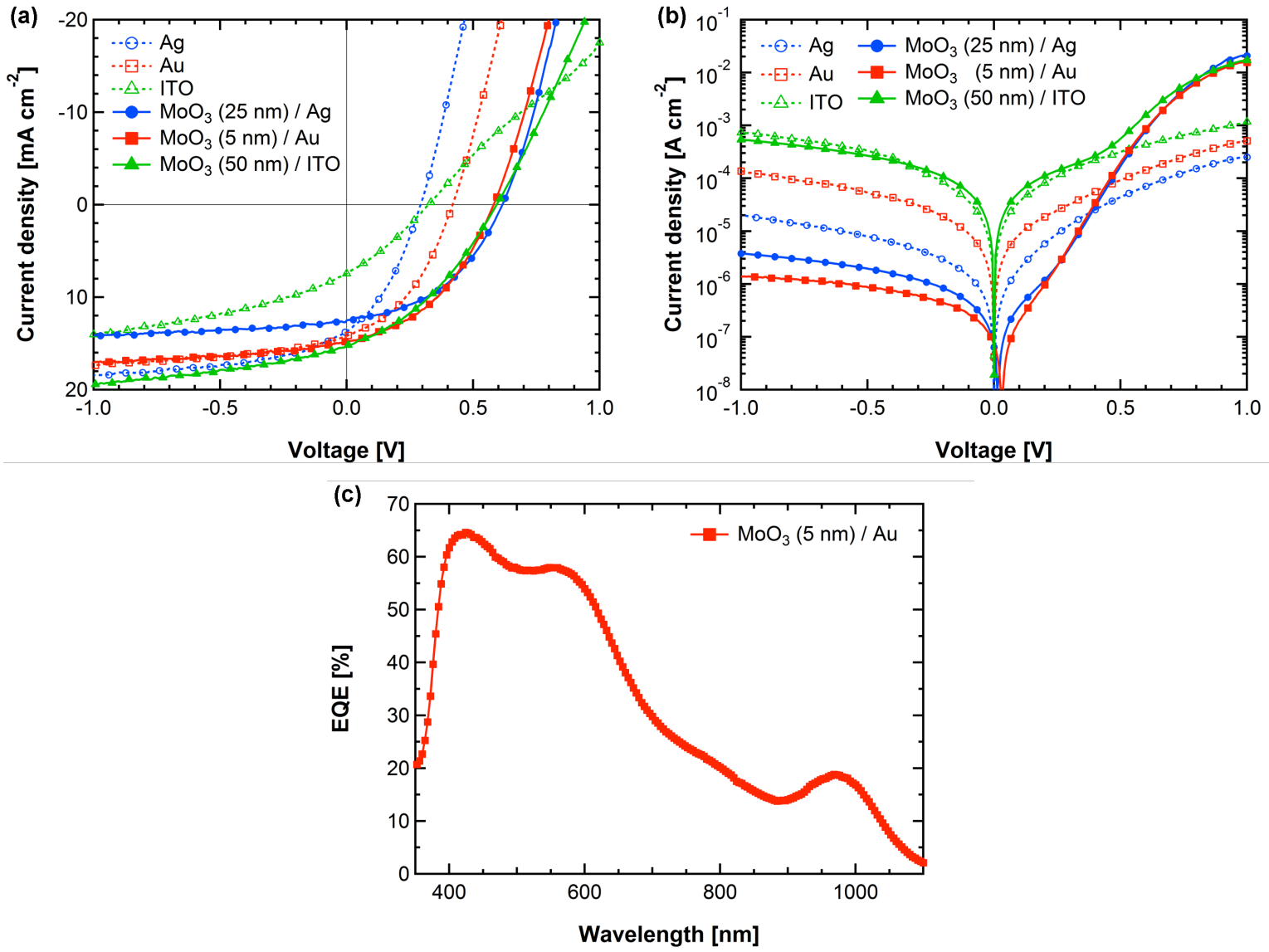

Figure 14. (a) *J-V* characteristics under illumination of representative ITO/ZnO/PbS/MoO_3/anode devices with varying thicknesses of MoO_3, where the anode is Ag (blue circles), Au (red squares), or ITO (green triangles). (b) Dark *J-V* characteristics of the same devices, showing an increase in forward bias dark current corresponding to a reduction of the Schottky barrier for holes. (c) EQE spectrum of a representative ITO/ZnO/PbS/MoO_3/Au device employing a 5 nm-thick layer of MoO_3. Integrating the product of the EQE with the AM1.5G solar spectrum yields a J_{SC} of 14.4 mA cm^{-2}, in close agreement with the measured J_{SC} of 14.8 mA cm^{-2}.

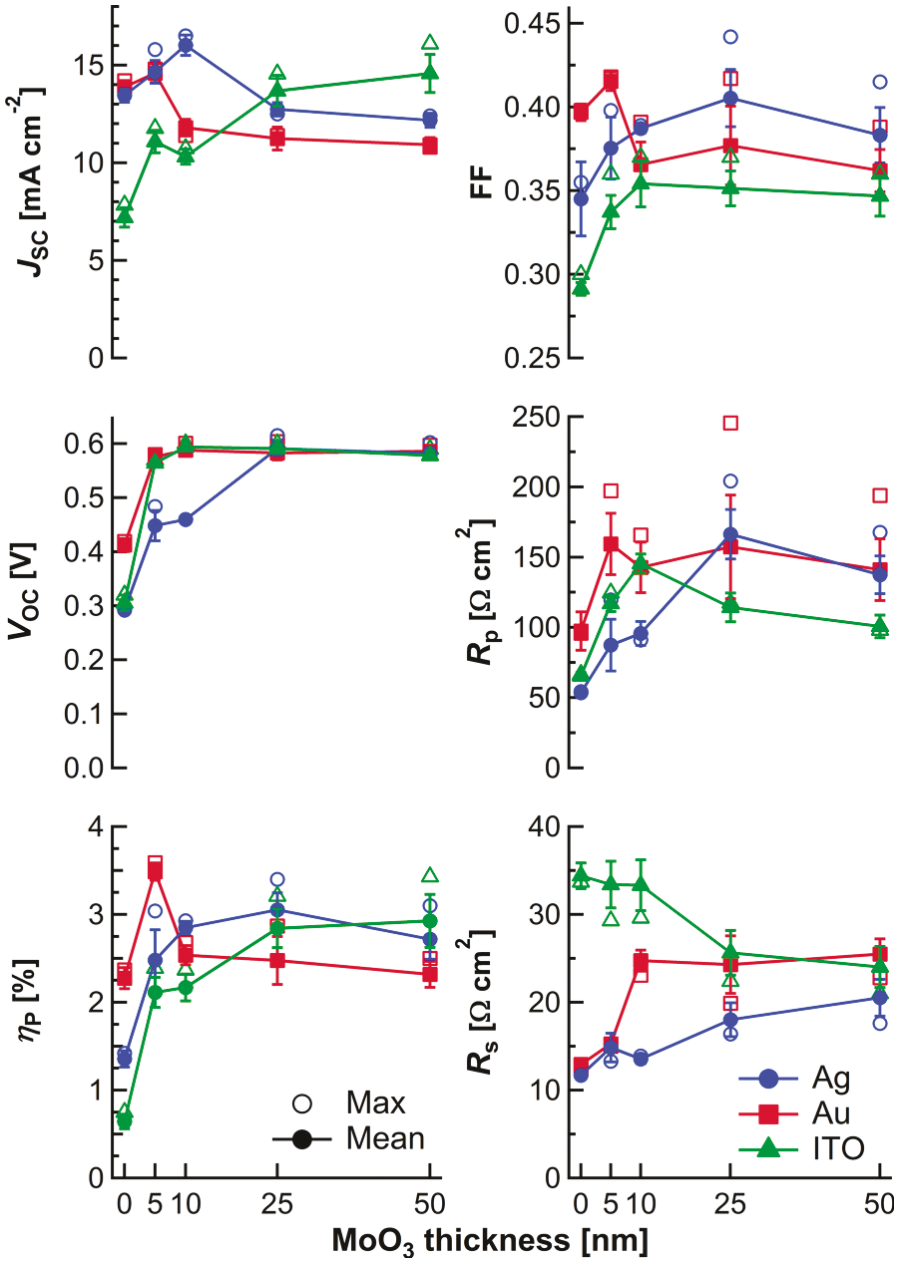

Figure 15. Device parameters of ITO/ZnO/PbS/MoO_3/anode devices as a function of MoO_3 thickness. Filled circles and error bars correspond to the average and standard deviation across eight to ten devices on the same substrate, and empty circles represent the value for the best-performing device. Lines serve as a guide to the eye. R_p and R_s are obtained from the inverse of the slope of the light *J-V* curve at $V = 0$ and $V = V_{OC}$, respectively.

A different trend is observed in the variation of J_{SC} and R_s with MoO_3 thickness for the three anode materials. For Au, a maximum in the J_{SC} occurs at a MoO_3 thickness of 5 nm, while for Ag, the maximum J_{SC} is obtained for 25 nm-thick MoO_3. For ITO, however, the J_{SC} continues to increase with increasing MoO_3 thickness, reaching a maximum at 50 nm-thick MoO_3. Optical simulations show that this increase in J_{SC} is not due to an interference effect

resulting from the addition of MoO_3 between the active layer and the anode. An increase in R_s is seen with increasing MoO_3 thickness for Ag and Au, while for ITO the R_s is observed to decrease for thicker MoO_3 layers. These opposing trends are possibly explained by the recent observance of a "dead zone" at the interface between PbS and sputtered ITO[59], resulting from damage to the underlying PbS layer induced by the high-energy reactive ions present during the ITO sputtering process. The MoO_3, which is thermally evaporated, is expected to act as a physical protective layer for the underlying PbS during sputtering of the ITO, with a thicker MoO_3 layer providing better protection and a correspondingly lower R_s and higher J_{SC}. The high V_{OC} and FF observed in Figure 13 for the device employing a thin, 46 nm layer of PbS suggests that MoO_3 is indeed effective in preventing damage to the PbS, although the low sputtering power used here (7W, vs. 30W used in reference 59) may also reduce the level of damage. Further work is necessary to characterize any chemical or structural changes at the PbS/anode interface if sputtered top electrodes are to be widely employed.

We note that the work function and band energies of MoO_3 presented in Figure 8 are under debate, with reported values differing by ± 1 eV for the work function and ± 4 eV for the electron affinity and ionization energy.[41,43,50] Much of this disagreement may stem from differences in measurement conditions, as Irfan *et al.*[61] and Meyer *et al.*[62] have shown that the work function of thermally evaporated MoO_3 decreases from 6.8 eV in ultra-high vacuum (UHV) to 5.7 eV after brief exposure to ambient pressure. The lower value for the work function is more representative of the MoO_3 employed here, as our devices are exposed to an inert atmosphere of nitrogen inside a glovebox between UHV deposition of the MoO_3 and anode layers. The observation of electron-blocking characteristics reported in organic photovoltaics[45] suggests a *p*-type character for MoO_3, where the MoO_3 functions to transport holes and block back-electron transfer from PbS to the anode; however, an *n*-type character for MoO_3, involving electron injection from the anode into MoO_3 and subsequent recombination of photogenerated holes and injected electrons at the PbS/MoO_3 interface, is more consistent with ultraviolet photoemission spectroscopy results reported elsewhere.[41] In FET measurements performed within this study, no field effect was observed for MoO_3, so an assignment of *n*-type or *p*-type character was unable to be made; nevertheless, a work function of ~5.7 eV, which is experimentally agreed upon for ambient-exposed MoO_3, would induce a similar change in the PbS energy levels regardless of the doping type.

Some previous reports on the incorporation of MoO_3 into photovoltaic devices have ascribed an increase in efficiency to a reduction in series resistance resulting from improved hole extraction from the *p*-type donor through the high-work function MoO_3,[44,54] while others have attributed it to a decrease in dark current and concomitant increase in shunt resistance, identifying an electron-blocking character as the primary contribution of MoO_3.[45,47] Both effects are observed in the present study, although the improvement in hole extraction resulting from removal of the top Schottky barrier plays the dominant role. For each of the three electrode materials, the shunt resistance is increased upon incorporation of MoO_3 (Figure 15), although the increase is not monotonic with MoO_3 thickness. This increase in shunt resistance reflects a general reduction in reverse-bias leakage current in the dark (Figure 14b), although the dark leakage current has also been observed to vary significantly without a strong effect on the light *J-V* characteristics. The key distinction between the devices described here without MoO_3 and those in reference 45 is a more pronounced crossover between the light and dark current in

forward bias (Figure 9). This deviation from ideal single-diode behavior indicates that a low forward bias current in the dark does not necessarily translate into a high V_{OC} in the light. Instead, the forward-bias dark current and the V_{OC} increase simultaneously upon incorporation of MoO_3 (Figures 14a-b). While an electron-blocking character for MoO_3 may still play a role, the polarity reversal and spectral shift of the ITO_P/PbS/ITO device in Figures 11 and 12 suggest that its primary impact on the device performance is due to the attenuation of the top-contact Schottky barrier. The crossover effect has been observed to varying degrees in organic-,[63] QD-,[38] CdS/Cu_2S-,[64] and CdS/CdTe-[65] photovoltaics, and has been attributed to a variety of factors. A more complete understanding of the determinants of this effect should lead to further improvements in V_{OC} and FF for QD photovoltaics.

In summary, the performance of ZnO/PbS QD heterojunction photovoltaics was significantly enhanced through engineering of the charge extraction barrier at the anode contact. The insertion of a MoO_3 thin film between the PbS active layer and the top-contacted anode improves the J_{SC}, V_{OC}, FF, and η_P simultaneously for a variety of anode materials. The high-work-function MoO_3 film pins the Fermi level of the anode contact and prevents the formation of a Schottky junction, which could impede the extraction of holes from PbS. We show that such a device structure decouples the device operation from the work function of the anode, allowing for the use of a transparent ITO top electrode to optically probe the different device interfaces during operation and potentially to aid in the future design of stacked tandem QD photovoltaics.

References

(1) Tang, C. W., 2-Layer Organic Photovoltaic Cell. *Appl. Phys. Lett.* **1986**, 48, 183-185.
(2) Peumans, P.; Uchida, S.; Forrest, S. R., Efficient Bulk Heterojunction Photovoltaic Cells Using Small-Molecular-Weight Organic Thin Films. *Nature* **2003**, 425, 158-162.
(3) Peumans, P.; Yakimov, A.; Forrest, S. R., Small Molecular Weight Organic Thin-Film Photodetectors and Solar Cells. *J. Appl. Phys.* **2003**, 93, 3693-3723.
(4) Xue, J. G.; Uchida, S.; Rand, B. P.; Forrest, S. R., 4.2% Efficient Organic Photovoltaic Cells with Low Series Resistances. *Appl. Phys. Lett.* **2004**, 84, 3013-3015.
(5) Chen, H.-Y.; Hou, J.; Zhang, S.; Liang, Y.; Yang, G.; Yang, Y.; Yu, L.; Wu, Y.; Li, G., Polymer Solar Cells with Enhanced Open-Circuit Voltage and Efficiency. *Nat. Photonics* **2009**, 3, 649-653.
(6) Giebeler, C.; Marks, R. N.; Bleyer, A.; Bradley, D. D. C.; Schrader, S., The Photovoltaic Effect in Poly(p-phenylene-2,3 '-bis(3,2 '-diphenyl)-quinoxaline-7-7 '-diyl). *Opt. Mater.* **1998**, 9, 99-103.
(7) Halls, J. J. M.; Walsh, C. A.; Greenham, N. C.; Marseglia, E. A.; Friend, R. H.; Moratti, S. C.; Holmes, A. B., Efficient Photodiodes From Interpenetrating Polymer Networks. *Nature* **1995**, 376, 498-500.
(8) Li, G.; Shrotriya, V.; Huang, J. S.; Yao, Y.; Moriarty, T.; Emery, K.; Yang, Y., High-Efficiency Solution Processable Polymer Photovoltaic Cells by Self-Organization of Polymer Blends. *Nat. Mater.* **2005**, 4, 864-868.
(9) Park, S. H.; Roy, A.; Beaupre, S.; Cho, S.; Coates, N.; Moon, J. S.; Moses, D.; Leclerc, M.; Lee, K.; Heeger, A. J., Bulk Heterojunction Solar Cells with Internal Quantum Efficiency Approaching 100%. *Nat. Photonics* **2009**, 3, 297-303.

(10) Gur, I.; Fromer, N. A.; Geier, M. L.; Alivisatos, A. P., Air-Stable All-Inorganic Nanocrystal Solar Cells Processed from Solution. *Science* **2005**, 310, 462-465.
(11) Huynh, W. U.; Dittmer, J. J.; Alivisatos, A. P., Hybrid Nanorod-Polymer Solar Cells. *Science* **2002**, 295, 2425-2427.
(12) Alivisatos, A. P., Semiconductor Clusters, Nanocrystals, and Quantum Dots. *Science* **1996**, 271, 933-937.
(13) Murray, C. B.; Norris, D. J.; Bawendi, M. G., Synthesis And Characterization Of Nearly Monodisperse Cde (E = S, Se, Te) Semiconductor Nanocrystallites. *J. Am. Chem. Soc.* **1993**, 115, 8706-8715.
(14) Dabbousi, B. O.; RodriguezViejo, J.; Mikulec, F. V.; Heine, J. R.; Mattoussi, H.; Ober, R.; Jensen, K. F.; Bawendi, M. G., (CdSe)ZnS Core-Shell Quantum Dots: Synthesis and Characterization of A Size Series of Highly Luminescent Nanocrystallites. *J. Phys. Chem. B* **1997**, 101, 9463-9475.
(15) Luther, J. M.; Law, M.; Beard, M. C.; Song, Q.; Reese, M. O.; Ellingson, R. J.; Nozik, A. J., Schottky Solar Cells Based on Colloidal Nanocrystal Films. *Nano Lett.* **2008**, 8, 3488-3492.
(16) Barkhouse, D. A. R.; Pattantyus-Abraham, A. G.; Levina, L.; Sargent, E. H., Thiols Passivate Recombination Centers in Colloidal Quantum Dots Leading to Enhanced Photovoltaic Device Efficiency. *Acs Nano* **2008**, 2, 2356-2362.
(17) Johnston, K. W.; Pattantyus-Abraham, A. G.; Clifford, J. P.; Myrskog, S. H.; MacNeil, D. D.; Levina, L.; Sargent, E. H., Schottky-Quantum Dot Photovoltaics for Efficient Infrared Power Conversion. *Appl. Phys. Lett.* **2008**, 92, 151115.
(18) Koleilat, G. I.; Levina, L.; Shukla, H.; Myrskog, S. H.; Hinds, S.; Pattantyus-Abraham, A. G.; Sargent, E. H., Efficient, Stable Infrared Photovoltaics Based on Solution-Cast Colloidal Quantum Dots. *Acs Nano* **2008**, 2, 833-840.
(19) Nelson, J., *The Physics of Solar Cells*. Imperial College Press: London, **2003**.
(20) Choi, J. J.; Lim, Y. F.; Santiago-Berrios, M. B.; Oh, M.; Hyun, B. R.; Sun, F.; Bartnik, A. C.; Goedhart, A.; Malliaras, G. G.; Abrua, H. D.; Wise, F. W.; Hanrath, T., PbSe Nanocrystal Excitonic Solar Cells. *Nano Lett.* **2009**, 9, 3749-3755.
(21) Leschkies, K. S.; Beatty, T. J.; Kang, M. S.; Norris, D. J.; Aydil, E. S., Solar Cells Based on Junctions between Colloidal PbSe Nanocrystals and Thin ZnO Films. *ACS Nano* **2009**, 3, 3638-3648.
(22) Rauch, T.; Boberl, M.; Tedde, S. F.; Furst, J.; Kovalenko, M. V.; Hesser, G. N.; Lemmer, U.; Heiss, W.; Hayden, O., Near-Infrared Imaging with Quantum-Dot-Sensitized Organic Photodiodes. *Nat. Photonics* **2009**, 3, 332-336.
(23) Szendrei, K.; Cordella, F.; Kovalenko, M. V.; Boberl, M.; Hesser, G.; Yorema, M.; Jarzab, D.; Mikhnenko, O. V.; Gocalinska, A.; Saba, M.; Quochi, F.; Mura, A.; Bongiovanni, G.; Blom, P. W. M.; Heiss, W. G.; Loi, M. A., Solution-Processable Near-IR Photodetectors Based on Electron Transfer from PbS Nanocrystals to Fullerene Derivatives. *Adv. Mater.* **2009**, 21, 683-687.
(24) Klem, E. J. D.; Shukla, H.; Hinds, S.; MacNeil, D. D.; Levina, L.; Sargent, E. H., Impact of Dithiol Treatment and Air Annealing on the Conductivity, Mobility, and Hole Density in PbS Colloidal Quantum Dot Solids. *Appl. Phys. Lett.* **2008**, 92, 212105.
(25) Luther, J. M.; Law, M.; Song, Q.; Perkins, C. L.; Beard, M. C.; Nozik, A. J., Structural, Optical and Electrical Properties of Self-Assembled Films of PbSe Nanocrystals Treated with 1,2-ethanedithiol. *Acs Nano* **2008**, 2, 271-280.

(26) Klem, E. J. D.; MacNeil, D. D.; Levina, L.; Sargent, E. H., Solution Processed Photovoltaic Devices with 2% Infrared Monochromatic Power Conversion efficiency: Performance Optimization and Oxide Formation. *Adv. Mater.* **2008**, 20, 3433-3439.
(27) Tang, J.; Brzozowski, L.; Barkhouse, D. A. R.; Wang, X.; Debnath, R.; Wolowiec, R.; Palmiano, E.; Levina, L.; Pattantyus-Abraham, A. G.; Jamakosmanovic, D.; Sargent, E. H., Quantum Dot Photovoltaics in the Extreme Quantum Confinement Regime: The Surface-Chemical Origins of Exceptional Air- and Light-Stability. *Acs Nano* **2010**, 4, 869-878.
(28) Konstantatos, G.; Levina, L.; Fischer, A.; Sargent, E. H., Engineering the Temporal Response of Photoconductive Photodetectors via Selective Introduction of Surface Trap States. *Nano Lett.* **2008**, 8, 1446-1450.
(29) Leatherdale, C. A.; Bawendi, M. G., Observation of Solvatochromism in CdSe Colloidal Quantum Dots. *Phys. Rev. B* **2001**, 63, 165315.
(30) Mihailetchi, V. D.; Wildeman, J.; Blom, P. W. M., Space-Charge Limited Photocurrent. *Phys. Rev. Lett.* **2005**, 94, 126602.
(31) O'Regan, B. C.; Scully, S.; Mayer, A. C.; Palomares, E.; Durrant, J., The Effect of Al2O3 Barrier Layers in TiO2/Dye/CuSCN Photovoltaic Cells Explored by Recombination and DOS Characterization Using Transient Photovoltage Measurements. *J. Phys. Chem. B* **2005**, 109, 4616-4623.
(32) Goh, C.; Scully, S. R.; McGehee, M. D., Effects of Molecular Interface Modification in Hybrid Organic-Inorganic Photovoltaic Cells. *J. Appl. Phys.* **2007**, 101, 114503.
(33) Snaith, H. J.; Moule, A. J.; Klein, C.; Meerholz, K.; Friend, R. H.; Gratzel, M., Efficiency Enhancements in Solid-State Hybrid Solar Sells via Reduced Charge Recombination and Increased Light Capture. *Nano Lett.* **2007**, 7, 3372-3376.
(34) Luther, J. M.; Gao, J.; Lloyd, M. T.; Semonin, O. E.; Beard, M. C.; Nozik, A. J. *Advanced Materials*. **2010**, *22*, 3704-3707.
(35) Pattantyus-Abraham, A. G.; Kramer, I. J.; Barkhouse, A. R.; Wang, X.; Konstantatos, G.; Debnath, R.; Levina, L.; Raabe, I.; Nazeeruddin, M. K.; Grätzel, M.; Sargent, E. H. *ACS nano*. **2010**, *4*, 3374-80.
(36) Ju, T.; Graham, R. L.; Zhai, G.; Rodriguez, Y. W.; Breeze, A. J.; Yang, L.; Alers, G. B.; Carter, S. a *Applied Physics Letters*. **2010**, *97*, 043106.
(37) Zarghami, M. H.; Liu, Y.; Gibbs, M.; Gebremichael, E.; Webster, C.; Law, M. *ACS nano*. **2010**, *4*, 2475-85.
(38) Gao, J.; Luther, J. M.; Semonin, O. E.; Ellingson, R. J.; Nozik, A. J.; Beard, M. C. *Nano letters*. **2011**, *11*, 1002-1008.
(39) Luther, J. M.; Law, M.; Beard, M. C.; Song, Q.; Reese, M. O.; Ellingson, R. J.; Nozik, A. J. *Nano letters*. **2008**, *8*, 3488-92.
(40) Pan, J.; Gloeckler, M.; Sites, J. R. *Journal of Applied Physics*. **2006**, *100*, 124505.
(41) Kröger, M.; Hamwi, S.; Meyer, J.; Riedl, T.; Kowalsky, W.; Kahn, A. *Applied Physics Letters*. **2009**, *95*, 123301.
(42) Matsushima, T.; Kinoshita, Y.; Murata, H. *Applied Physics Letters*. **2007**, *91*, 253504.
(43) Shrotriya, V.; Li, G.; Yao, Y.; Chu, C.-W.; Yang, Y. *Applied Physics Letters*. **2006**, *88*, 073508.
(44) Kim, D.; Y. Subbiah, J.; Sarasqueta, G.; So, F.; Ding, H.; Gao, Y. *Applied Physics Letters*. **2009**, *95*, 093304.

(45) Li, N.; Lassiter, B. E.; Lunt, R. R.; Wei, G.; Forrest, S. R. *Applied Physics Letters*. **2009**, *94*, 023307.
(46) Hancox, I.; Chauhan, K. V.; Sullivan, P.; Hatton, R. A.; Moshar, A.; Mulcahy, C. P. A.; Jones, T. S. *Energy & Environmental Science*. **2010**, *3*, 107.
(47) Tao, C.; Ruan, S.; Zhang, X.; Xie, G.; Shen, L.; Kong, X.; Dong, W.; Liu, C.; Chen, W. *Applied Physics Letters*. **2008**, *93*, 193307.
(48) Lee, J. H.; Cho, S.; Roy, A.; Jung, H.-T.; Heeger, A. J. *Applied Physics Letters*. **2010**, *96*, 163303.
(49) Sun, Y.; Takacs, C. J.; Cowan, S. R.; Seo, J. H.; Gong, X.; Roy, A.; Heeger, A. J. *Advanced Materials*. **2011**, Early View.
(50) Qi, X.; Li, N.; Forrest, S. R. *Journal of Applied Physics*. **2010**, *107*, 014514.
(51) Leschkies, K. S.; Beatty, T. J.; Kang, M. S.; Norris, D. J.; Aydil, E. S. *ACS nano*. **2009**, *3*, 3638-48.
(52) Park, Y.; Choong, V.; Gao, Y.; Hsieh, B. R.; Tang, C. W. *Applied Physics Letters*. **1996**, *68*, 2699.
(53) Hyun, B.-R.; Zhong, Y.-W.; Bartnik, A. C.; Sun, L.; Abruña, H. D.; Wise, F. W.; Goodreau, J. D.; Matthews, J. R.; Leslie, T. M.; Borrelli, N. F. *ACS nano*. **2008**, *2*, 2206-12.
(54) Lin, H.; Xia, W.; Wu, H. N.; Tang, C. W. *Applied Physics Letters*. **2010**, *97*, 123504.
(55) Bube, R. H.; Fahrenbruch, A. L. *Advances in Electronics and Electron Physics*; Academic: New York, 1981; p. 163.
(56) Johnston, K.; W. Pattantyus-Abraham, A. G.; Clifford, J. P.; Myrskog, S. H.; MacNeil, D. D.; Levina, L.; Sargent, E. H. *Applied Physics Letters*. **2008**, *92*, 151115.
(57) Park, Y.; Choong, V.; Gao, Y.; Hsieh, B. R.; Tang, C. W. *Applied Physics Letters*. **1996**, *68*, 2699.
(58) Milliron, D. J.; Hill, I. G.; Shen, C.; Kahn, A.; Schwartz, J. *Journal of Applied Physics*. **2000**, *87*, 572.
(59) Barkhouse, D. A. R.; Kramer, I. J.; Wang, X.; Sargent, E. H. *Optics express*. **2010**, *18*, A451-7.
(60) Michaelson, H. B. *Journal of Applied Physics*. **1977**, *48*, 4729-4733.
(61) Irfan; Ding, H.; Gao, Y.; Small, C.; Kim, D. Y.; Subbiah, J.; So, F. *Applied Physics Letters*. **2010**, *96*, 243307.
(62) Meyer, J.; Shu, A.; Kröger, M.; Kahn, A. *Applied Physics Letters*. **2010**, *96*, 133308.
(63) Nelson, J. Kirkpatrick, J.; Ravirajan, P. *Physical Review B*. **2004**, *69*, 1-11.
(64) Pfisterer, F. *Thin Solid Films*. **2003**, *431-432*, 470-476.
(65) Poortmans, J.; Arkhipov, V. *Thin Film Solar Cells Fabrication , Characterization and Applications*; John Wiley & Sons, Ltd: West Sussex, England, 2006.

Publications generated during this program:

1) M.R. Hummon, A.J. Stollenwerk, V. Narayanamurti, P.O. Anikeeva, M.J. Panzer, V. Wood, V. Bulović, “Measuring Charge Trap Occupation and Energy Level in CdSe/ZnS Quantum Dots Using a Scanning Tunneling Microscope,” *Physical Review B* 81, 115439 (2010).

2) N. Zhao, T.P. Osedach, L.-Y. Chang, S.M. Geyer, D. Wanger, M.T. Binda, A.C. Arango, M.G. Bawendi, V. Bulović, “Colloidal PbS Quantum Dot Solar Cells with High Fill Factor,” *ACS Nano* 4, 3743-3752 (2010).

3) T.P. Osedach, N. Zhao, S.M. Geyer, L.Y. Chang, D.D. Wanger, A.C. Arango, M.G. Bawendi, V. Bulović, “Interfacial Recombination for Fast Operation of a Planar Organic/QD Infrared Photodetector,” *Advanced Materials* 22, 5250-5254 (2010).

4) P.R. Brown, R.R. Lunt, N. Zhao, T.P. Osedach, D.D. Wanger, L.Y. Chang, M.G. Bawendi, V. Bulović, “Improved current extraction from ZnO/PbS quantum dot heterojunction photovoltaics using MoO3 interfacial layer,” *Nano Letters* 11, 2955-2961 (2011).

Student/Postdoc Conference Presentations:

1) N. Zhao, *et al.* "Infrared Solar Cells Based on a Colloidal Quantum Dots/Organic Bilayer Structure," 2010 Spring Meeting of the Materials Research Society, San Francisco CA (April 2010).

2) T.P. Osedach, N. Zhao, S.M. Geyer, L.-Y. Chang, D. Wanger, A.C. Arango, M.G. Bawendi, V. Bulović, "Fast Operation of SWIR Organic/QD Photodetector via Interfacial Recombination," International Conference on Organic Electronics, Paris, France (June 2010).

3) N. Zhao, T. P. Osedach, L.Y. Chang, S. M. Geyer, M. G. Bawendi, V. Bulovic, “Towards Efficient Infrared Quantum Dot Photovoltaic Cells,” Optics and Photonics for Advanced Energy Technology Conference, Cambridge, MA, June, 2009.

4) Brown, P. R.; Lunt, R. R.; Zhao, N.; Osedach, T. P.; Wanger, D. D.; Chang, L.-Y.; Bawendi, M. G.; Bulović, V. “Improved current extraction from ZnO/PbS quantum dot heterojunction photovoltaics using a MoO3 interfacial layer,” 2011 Fall Meeting of the Materials Research Society, Boston, MA (Novemebr 2011).

5) Brown, P. R.; Lunt, R. R.; Zhao, N.; Osedach, T. P.; Wanger, D. D.; Chang, L.-Y.; Bawendi, M. G.; Bulović, V. “Improved current extraction from quantum dot heterojunction photovoltaics using a metal oxide interfacial layer,” Microsystems

Technology Laboratory Annual Research Conference, contributed oral/poster presentation, Waterville Valley, MA (January 2012).

6) Brown, P. R.; Lunt, R. R.; Zhao, N.; Osedach, T. P.; Wanger, D. D.; Chang, L.-Y.; Bawendi, M. G.; Bulović, V. “Improved current extraction from ZnO/PbS quantum dot heterojunction photovoltaics using a MoO3 interfacial layer,” 7th International Conference on Quantum Dots, accepted for contributed poster presentation, Santa Fe, NM (May 2012).

Invited Lectures Inspired by the outputs of this research program:

1) V. Bulović, Conference on Clean Energy, Boston, MA, November 2010.

2) V. Bulović, 2011 Kentucky Statewide Workshop: Renewable Energy & Energy Efficiency, Louisville, KY, March 2011.

3) V. Bulović, Wellesley College – Panel on Energy Technologies, April 2011.

4) V. Bulović, National Renewable Energy Lab, Golden CO, June 2011.

5) V. Bulović, University of Colorado, Boulder CO, June 2011.

6) V. Bulović, 220th ECS Meeting, Grand Challenges in Energy Conversion and Storage, Boston MA , October 2011.

7) V. Bulović, American Physical Society Meeting, Boston MA, February 2012.